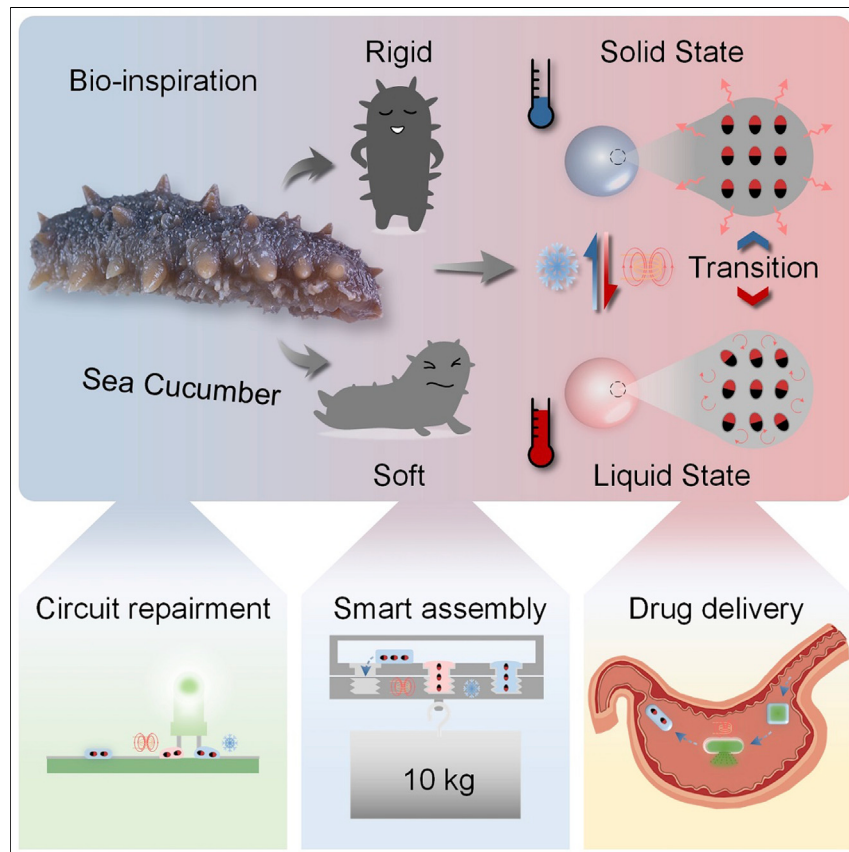


Article

Magnetoactive liquid-solid phase transitional matter



Magnetoactive phase transitional matter that is composed of NdFeB microparticles embedded in liquid metal can achieve high mechanical strength (stiffness, 1.98 GPa), high load capacity, fast and multimodal locomotion (jumping up to 20× body length, moving up to 1.5 m/s) in its solid state, and excellent morphological adaptability (elongation, splitting, and merging) in its liquid state. This stimuli-responsive material architecture enables new applications in flexible electronics, robotics, and healthcare.

Qingyuan Wang, Chengfeng Pan, Yuanxi Zhang, Lelun Peng, Zhipeng Chen, Carmel Majidi, Lelun Jiang

cmajidi@andrew.cmu.edu (C.M.)
jiangle@mail.sysu.edu.cn (L.J.)

Highlights

Magnetoactive phase transitional matter (MPTM) is made of NdFeB embedded liquid metal

MPTMs can reversibly switch between solid and liquid phase

MPTMs can solder electronic components and assemble parts in hard-to-reach space

MPTMs can remove foreign objects or deliver drugs in a model stomach

4

Demonstrate

Proof-of-concept of performance with intended application/response

Article

Magnetoactive liquid-solid phase transitional matter

Qingyuan Wang,^{1,5} Chengfeng Pan,^{2,3,5} Yuanxi Zhang,¹ Lelun Peng,¹ Zhipeng Chen,¹ Carmel Majidi,^{3,*} and Lelun Jiang^{1,4,*}

SUMMARY

Magnetically actuated miniature machines can perform multimodal locomotion and programmable deformations. However, they are either solid magnetic elastomers with limited morphological adaptability or liquid material systems with low mechanical strength. Here, we report magnetoactive phase transitional matter (MPTM) composed of magnetic neodymium-iron-boron microparticles embedded in liquid metal. MPTMs can reversibly switch between solid and liquid phase by heating with alternating magnetic field or through ambient cooling. In this way, they uniquely combine high mechanical strength (strength, 21.2 MPa; stiffness, 1.98 GPa), high load capacity (able to bear 30 kg), and fast locomotion speed (>1.5 m/s) in the solid phase with excellent morphological adaptability (elongation, splitting, and merging) in the liquid phase. We demonstrate the unique capabilities of MPTMs by showing their dynamic shape reconfigurability by realizing smart soldering machines and universal screws for smart assembly and machines for foreign body removal and drug delivery in a model stomach.

INTRODUCTION

Untethered miniature machines have shown tremendous potential in various fields, such as targeted drug delivery,^{1–4} lab-/organ-on-a-chip,^{5–8} and microelectronics.^{9–12} Compared with miniature machines actuated by light, electric field, chemicals, and other stimuli, magnetic-field-driven systems are capable of fast and precise controllability, programmable locomotion, and untethered operation without the need for line-of-site with the stimulation source.¹³ Recently, researchers have put tremendous effort into increasing the mobility, controllability, and morphological adaptability of magnetically actuated machines to broaden their applications. One common class of magnetically actuated miniature machines is composed of soft polymers (e.g., elastomers or hydrogels) embedded with ferromagnetic particles that are engineered with a programmed magnetization profile.^{14–18} These machines can achieve multimodal locomotion^{14,15} (swimming, climbing, rolling, walking, and jumping) or predefined complex three-dimensional (3D) shape changing^{16–18} driven by induced magnetic torque under corresponding magnetic fields. Such untethered miniature machines can gain access to confined and hard-to-reach spaces, such as cavities or organs within the human body,^{19,20} and accomplish multiple tasks including targeted cargo delivery,¹⁷ non-invasive medical diagnosis,^{4,21–24} and therapy for healing ulcers.²⁵ However, these elastomer-based composites are difficult to navigate through very narrow and confined spaces with openings smaller than the dimensions of the material. This is due to the solid nature and limited deformability of such elastic material systems.

PROGRESS AND POTENTIAL

This study presents a class of magnetoactive phase transitional matter (MPTM). MPTMs exhibit a combination of high mechanical strength, high load capacity, fast locomotion, excellent controllability, and robust morphological adaptability. This unique combination of properties is enabled by the reversible transition of MPTMs between rigid and fluidic states through alternating magnetic field heating and ambient cooling. To illustrate the unique capabilities of MPTMs, we demonstrate smart soldering machines to manipulate and solder electronic components to create a functional circuit. We also use MPTMs as universal screws to assemble parts in hard-to-reach space and as a capsule machine for removing foreign objects or delivering drugs in a model stomach. MPTMs are promising for future applications in flexible electronics, healthcare, and robotics that depend on dynamic shape reconfigurability and repair.

In contrast to these solid material systems, magnetically actuated liquid-based machines^{26–31} exhibit much greater morphological adaptability for tasks such as passing through narrow and constrained spaces. For example, Fan et al.³² presented the ability for miniature droplets of ferrofluid to perform reconfigurable morphological transformation including elongation, splitting, merging, and transition into a ring shape.

Kim and colleagues^{33,34} investigated the magnetic-field-driven motion of ferromagnetic liquid metal (LM) droplets through microfluidic channels embedded within a soft silicone elastomer matrix. Li et al.³⁵ reported that the precise control and climbing locomotion of functional LM is demonstrated by the interworking of both electric and magnetic fields simultaneously. Liu et al.³⁶ demonstrated LM micromachines capable of dramatic morphological transformation in an aqueous environment. Magnetically actuated micromachine swarms also express a liquid-like property in terms of the morphological transformation of the whole group through their unique collective behaviors.^{37,38} For example, Sun et al.³⁹ demonstrated ferrofluid micromachine swarms that could navigate through multiple terrains such as curved grooves and narrow channels and achieve a dexterous “octopus arm”-like micromanipulator to grasp a targeted object through a confined space. However, such liquid-based machines or liquid-like micromachine swarms provide limited load capacity because of the poor mechanical strength of fluidic bodies.⁴⁰ Moreover, although magnetically actuated liquids exhibit excellent morphological flexibility and adaptability, high-speed locomotion is still challenging to achieve because of their low mobility and requirements for sophisticated systems to control the magnetic field.

To both support high load capacity and achieve morphological adaptability, natural organisms typically rely on dynamic stiffness changes. For example, the sea cucumber can reversibly alter the stiffness of its tissue in order to improve its load capacity and prevent physical damage from the environment (Figure 1A).⁴¹ An octopus can switch the stiffness of its arms between extreme compliance for dramatic morphological change and high stiffness for load-intensive tasks such as grasping, object manipulation, and locomotion (e.g., walking and crawling) (Figure 1A).^{42,43} Inspired by nature, researchers have explored stiffness tuning using a variety of material systems and strategies. This includes the use of quasi-solid magnetically actuated machines composed of phase-changeable polymer embedded with magnetic microparticles.^{44–50} In this way, the magnetic profile of the quasi-solid machine (i.e., composite sheet) can be dynamically reprogrammed through laser-controlled heating to trigger the glassy phase transition of the polymer matrix and then, using an electromagnetic field, alter the magnetization direction of the embedded magnetic particles.⁴⁴ Although this approach introduces shape-morphing capabilities and functionality (such as stiffness tuning), the morphological adaptability of these material systems is still limited because of their quasi-solid character (especially when the polymer matrix is in its glassy state) and inability to match the rheology of liquid-based magnetically actuated machines. In general, magnetically actuated machines are solid and quasi-solid machines with limited morphological adaptability or are liquid or paste-like with low mechanical strength (i.e., load capacity), poor mechanical integrity, poor controllability, and low locomotion speed. Combining fast locomotion with high mechanical strength (load capacity) and versatile morphological adaptability remains a major challenge in the development of magnetically actuated miniature machines.

In this work, we present a class of magnetoactive phase transitional matter (MPTM) to make phase-changing magnetic machines that are capable of achieving rapid and

¹Guangdong Provincial Key Laboratory of Sensor Technology and Biomedical Instruments, School of Biomedical Engineering, Shenzhen Campus of Sun Yat-sen University, Shenzhen 518107, P.R. China

²The State Key Laboratory of Fluid Power and Mechatronic Systems, College of Mechanical Engineering, Zhejiang University, Hangzhou 310027, P.R. China

³Soft Machines Lab, Mechanical Engineering, Carnegie Mellon University, Pittsburgh, PA 15213, USA

⁴Lead contact

⁵These authors contributed equally

*Correspondence:

cmajidi@andrew.cmu.edu (C.M.),
jiangle@mail.sysu.edu.cn (L.J.)

<https://doi.org/10.1016/j.matt.2022.12.003>

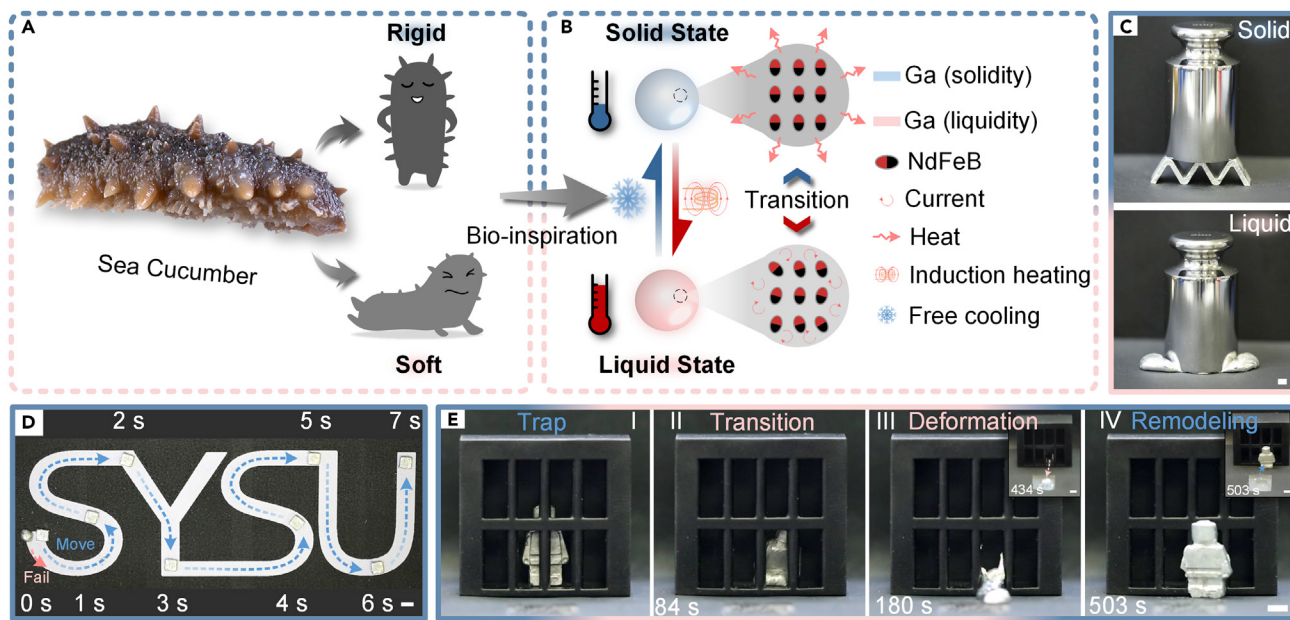


Figure 1. Schematic and applications of the liquid-solid phase transition of MPTM

(A) Photograph of a sea cucumber and schematic illustration of its stiffness-changing behavior.
(B) Illustration of the transition between solid and liquid phase of MPTM. Elliptic particles represent the magnetic orientation alignment of the NdFeB microparticles.
(C) Photos showing that solid MPTM can support a 200-g weight but liquid MPTM cannot. Scale bars, 3 mm.
(D) Photos showing that solid MPTM can pass along a path within 7 s showing excellent mobility and controllability, whereas a liquid-phase MPTM can hardly move. Scale bars, 3 mm.
(E) Photos showing MPTM using solid-liquid transformation to get out of a cage and restore its original shape. Scale bars, 3 mm.

reversible transitions between solid and liquid phase (Figure 1B). These phase transitional machines are made of ferromagnetic neodymium-iron-boron (NdFeB) microparticles embedded within a matrix of low-melting-point LM⁵¹ (e.g., Galinstan, -19°C; EGaIn, 15.7°C; gallium, 29.8°C; Bi₄₅Sn₂₃In₁₉Sn₈Cd₅, 47°C) and can switch phase through inductive heating by applying alternating magnetic field (AMF) heating and ambient cooling at room temperature. In the solid phase, the machines exhibit excellent mechanical strength (gallium based: strength, 21.2 MPa; modulus, 1.98 GPa) that enables high load capacity (Figure 1B). The stable magnetization of the embedded microparticles also enables more versatile mobility, including both fast movement (Figure 1D and Video S1) and multimodal locomotion (e.g., jumping, moving, and rotation). In the liquid phase, the material is fluidic and the magnetic microparticles are able to rotate and reorient their magnetic polarity to achieve morphological adaptations (Figure 1E) by elongating, dividing, and merging. We demonstrate the potential applications of this phase transitional machine through the following series of examples: (1) shape-reconfigurable matter that escape from a cage (Figure 1E and Video S2); (2) a smart soldering machine that manipulates and fuses electronic components for circuit assembly and repair; (3) a “universal” mechanical screw for assembling parts in a confined space; (4) a minimally invasive machine that removes a foreign object from within a model stomach; and (5) a capsule machine that provides on-demand drug delivery in a model stomach. This MPTM with unique combination of high mechanical strength, high load capacity, fast locomotion, excellent controllability, and robust morphological adaptability has great potential to further advance the design and development of miniature robots for various applications.

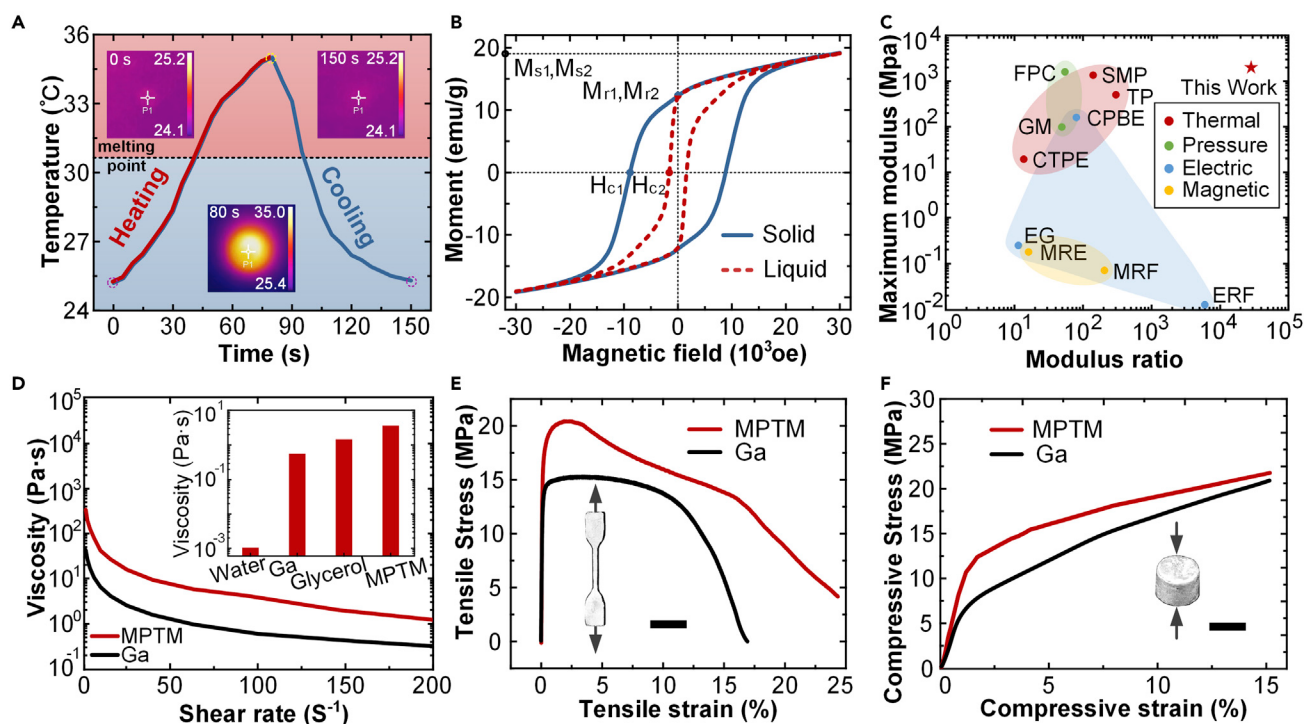


Figure 2. Characterization of MPTM

- (A) Temperature change of MPTM as a function of the heating and cooling time. Inset: infrared images.
- (B) Magnetic hysteresis loop of MPTM.
- (C) Maximum effective modulus and modulus ratio of MPTM and traditional phase-change materials (for details see Table S1).
- (D) Viscosity of liquid MPTM and Ga at different shear rates. Inset: viscosity of water, gallium, MPTM, and glycerin.
- (E) Stress-strain curves of tensile test of dogbone-shaped object. Scale bars, 10 mm.
- (F) Stress-strain curves of the compression test of the cylindrical object. Scale bars, 2 mm.

RESULTS AND DISCUSSION

Solid-liquid phase transitional matter

The MPTM is fabricated by mixing ferromagnetic NdFeB microparticles into a low-melting-point LM (pure gallium) matrix (Figures 1B and S1). Mechanical mixing is a common method to prepare LM particle composites.⁵² As the scanning electron microscopy (SEM) and energy-dispersive spectroscopy (EDS) images show in Figure S2, NdFeB microparticles are embedded within the gallium matrix without alloying, indicating clear phase separation of the NdFeB and gallium. Pure gallium was utilized as the LM matrix, since gallium has a melting point (29.8°C) that is close to room temperature and thereby enables rapid solid-liquid phase transition in ambient conditions (Figures 2A and S3A). We can tailor the phase transition temperature to cover a wide range for different applications by using LM alloys with different melting points, such as gallium-indium-tin ("Galinstan") (-19°C), eutectic gallium and indium ("EGaIn") (Ga₇₅In₂₅, 15.7°C), gallium-base alloy (In₅₃Bi₂₅Sn₁₄ Ga₈), Field's metal (Bi_{32.5}Sn_{16.5}In₅₁, 62°C), and bismuth-tin alloy (Bi₅₈Sn₄₂, 138°C).⁵³ The MPTM machine will remain in a solid state at room temperature because the melting point of the NdFeB-Ga composite is 30.6°C (Figure S3A). As shown in Figure 1C, solid MPTM is able to bear a relatively heavy object that is about 30 times its own weight, thereby demonstrating its high stiffness and mechanical strength. The solid gallium matrix will also constrain the embedded NdFeB microparticles from moving or rotating, thereby allowing the solid MPTMs to maintain a fixed, stable magnetic polarity (remnant magnetization 12 emu/g, coercivity

10,200 Oe). As shown in [Figure 1D](#), such material integrity allows a solid MPTM to move along a circuitous path (formed from the letters "SYSU") within 6 s. In contrast, a liquid-phase MPTM is observed to hardly move. We use AMF to heat the gallium matrix and trigger transition from the solid to liquid phase, thereby allowing for morphological adaptability. As shown in [Figure 1E](#), a MPTM figurine molded in the shape of a Lego minifigure escapes from a cage by transitioning to a liquid phase and being pulled through the cage bars by an external magnetic field. After escaping, the liquid MPTM restores its original shape by flowing into a mold. The phase transition behavior of MPTM under heating and cooling was investigated by measuring the temperature change of the machine. AMF and natural heat dissipation to the surrounding environment through convection were used for heating and cooling, respectively. During operation, the temperature of the MPTM (50 mg) is elevated from a room temperature of 25°C to 35°C and then returned back to 25°C. This corresponds to the phase state changing from solid to liquid and then back to solid within 80 and 70 s, respectively ([Figure 2A](#)). This temperature profile is consistent with the simulation results by finite element analysis (FEA) ([Figures 2A](#) [dashed line] and [S4](#); [Video S3](#)). These results show that MPTMs can achieve phase transition between solid and liquid state rapidly and reversibly.

The magnetically responsive behaviors of MPTMs in solid and liquid phase were investigated by measuring the magnetic hysteresis loop using a vibrating sample magnetometer (VSM) ([Figure 2B](#)). The large magnetic saturation intensity ($M_{s1} = M_{s2} = 19$ emu/g) and remnant magnetization ($Mr_1 = Mr_2 = 12$ emu/g) indicate that MPTMs in both the solid and liquid phase exhibit excellent ferromagnetic properties due to the initial saturated magnetization of NdFeB microparticles enabled by a 3 T pulsed magnetic field. However, the coercivity of solid MPTM (H_{c1}) is 10,200 Oe, which is 12 times larger than the coercivity of the liquid ($H_{c2} = 840$ Oe). Because the embedded NdFeB microparticles are constrained by the surrounding LM matrix in its solid phase, the magnetic polarity of the solid MPTM is fixed ([Figure 1B](#)). However, when the matrix is in the liquid phase, the NdFeB microparticles can change their orientation such that their magnetic polarity will be alternated by an external magnetic field ([Figure 1B](#)). The orientation and distribution of magnetic particles in matrix can be easily changed. Thus, MPTMs in the solid phase will be more responsive to magnetic actuation. [Figure S5A](#) shows that the saturated magnetization value and remnant magnetization increase through adding the NdFeB microparticles.

MPTMs exhibit an enabling combination of fluidity in the liquid phase and rigidity in the solid state, which correspond to a modulus change of nearly four orders of magnitude, far larger than most stiffness-tuning systems composed of phase-change materials ([Figure 2C](#)). We first studied the rheological properties of liquid-phase MPTM by measuring its viscosity at different shear rates. The results in [Figure 2D](#) show that the liquid-phase MPTM still exhibits excellent fluidity (shear rate 100 s⁻¹ to viscosity 3.83 Pa s) although increased viscosity compared with the LM matrix alone. This is due to the magnetic interaction between embedded NdFeB microparticles and interfacial interactions between the microparticles and surrounding LM matrix. The viscosity of gallium and MPTM is 0.58 and 3.83 Pa s (shear rate: 100 s⁻¹), respectively. For comparison, the viscosity of MPTM is close to that of glycerin (1.5 Pa s at 20°C) ([Figure 2D](#), inset). The results in [Figures S5B](#) and [S6](#) show that the viscosity and storage modulus increase through adding the NdFeB microparticles. Photos show that liquid MPTM can flow out of a pipette tip ([Figure S7](#)). The mechanical properties of solid MPTMs were investigated by recording the tensile and compressive stress-strain curves shown in [Figures 2E](#) and [2F](#). The results show that solid MPTMs exhibit strong material integrity, with a measured

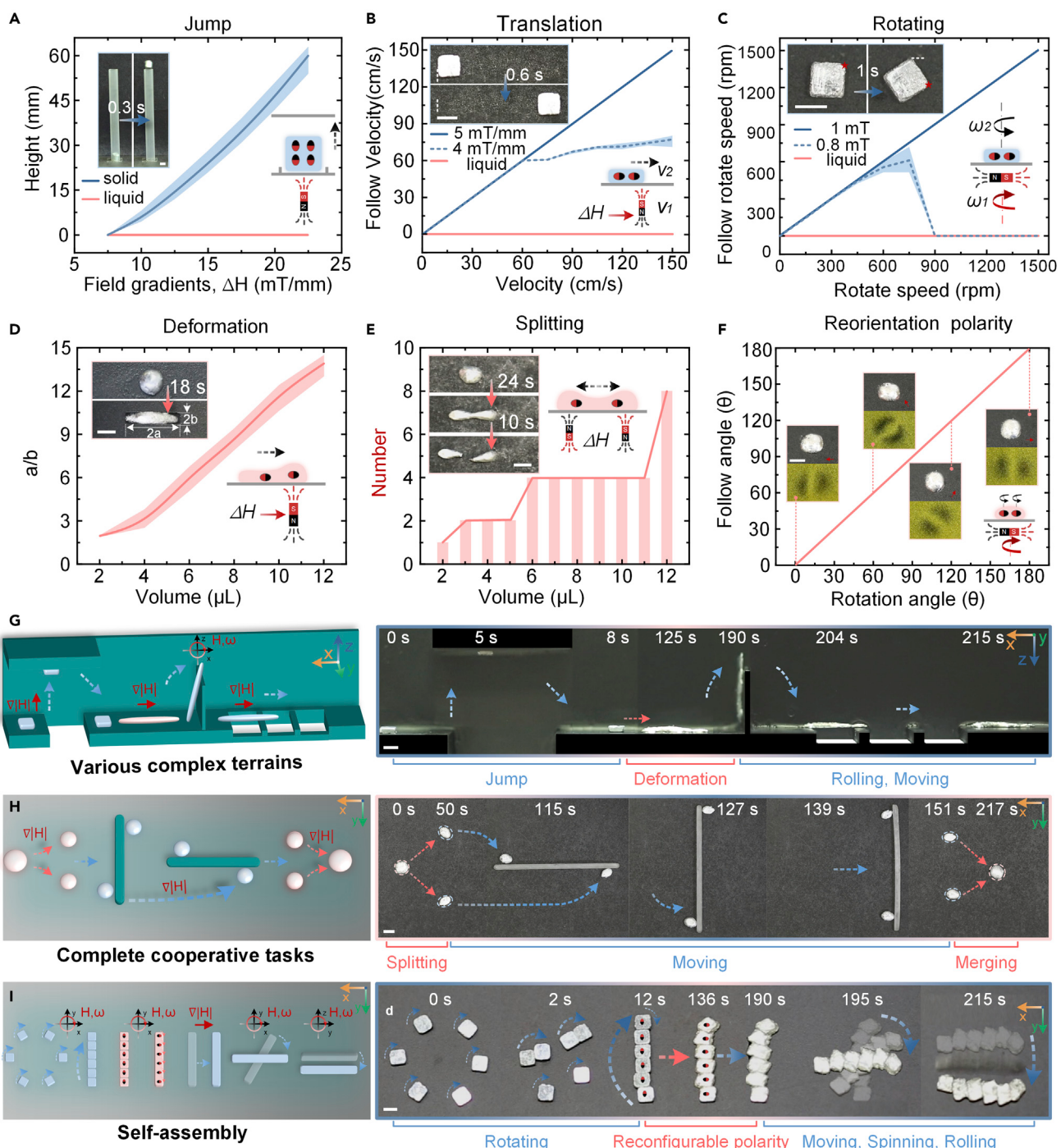


Figure 3. Typical magnetically actuated behaviors of solid and liquid MPTMs

(A) The maximum jumping height h_1 for solid MPTM and liquid MPTM with different field gradients ΔH . Sequential optical images and schematic illustration of the solid MPTM jump when subjected to gradient magnetic fields. The shaded areas indicate the SD of the results from six jumping tests.

(B) Characterization of the velocity v_2 of solid MPTM for different permanent magnet velocity v_1 . Sequential optical images and schematic illustration of the solid MPTM and liquid MPTM show the translation when subjected to gradient magnetic fields.

(C) Characterization of rotate speed ω_2 of solid MPTM and liquid MPTM for different driving speed ω_1 . Sequential optical images and schematic illustration of the solid MPTM rotating process when the rotating magnetic field parallel to the xy surface is applied.

(D) Deformability (a/b) of the liquid MPTM as a function of MPTM volume. Optical images of liquid MPTM before and after deformation. Schematic illustration of liquid MPTM deformation when subjected to gradient magnetic fields.

Figure 3. Continued

(E) Maximum splitting number of liquid MPTM as a function of MPTM volume. Sequential optical images and schematic illustration of liquid MPTM splitting process when subjected to gradient magnetic fields.

(F) Characterization of the polarity angles of liquid MPTMs follows that of external magnetic fields. Sequential optical images of the liquid MPTM reconfigurable polarity process. Surface magnetic field distributions of liquid MPTM characterization by magnetic display card. Red arrows represent the polarization direction of the magnetic field. Schematic illustration of the internal magnetic particle rotating process when the rotating magnetic field parallel to the xy surface is applied.

(G–I) Demonstration of complex functions achieved by multiple solid-liquid transition, such as (G) crossing various complex terrains, (H) splitting to complete cooperative tasks, and (I) self-assembly.

All scale bars represent 3 mm.

tensile strength, compressive strength, and elastic modulus of 21.2 MPa, 18.8 MPa, and 1.98 GPa, respectively. [Figure S8](#) shows the mechanical testing setups for obtaining these measurements.

MPTM mobility

Robust and versatile mobility represents a key objective of magnetically responsive miniature machines. We first investigated the fast locomotion capabilities and ability to control the motion of solid MPTMs by conducting jumping, moving, and rotating tests ([Figures 3A–3C](#) and [Video S4](#)). To clearly show the transformation and locomotion of the material, dark paper was used as the background in the experiment, and the complex scene was produced in commercial resin. [Figure S9](#) shows the adhesion of MPTM to the surface. [Figure S10](#) shows simulation results of a rotating magnetic field and gradient magnetic field under a motion test. It is well known that like poles repel each other. For the jumping tests, we approached the MPTM ($3 \times 3 \times 1$ mm, [Figure S11](#)) vertically from above with permanent magnets of various magnetic strengths. When the magnet was sufficiently close, the MPTM sample was observed to jump. Using this setup, we recorded the maximum jumping height as a function of the magnetic strength of the external magnet ([Figure 3A](#)). Solid MPTMs can achieve jumping heights of 60 mm (3 mm body length) by using magnets with a 22.5 mT/mm magnetic strength and can jump even higher under more powerful magnets. In contrast, liquid-phase MPTMs did not exhibit a jumping response. To explain the magnetic driving mechanism, [Figure S12](#) presents forces and free-body diagrams for the typical magnetic driving behavior of solid and liquid MPTMs.

We next tested the translation locomotion capability of solid MPTMs by driving the machines with a permanent magnet at different speeds on a flat surface and recording the translation speed of machines ([Figure 3B](#)). The results show that solid MPTMs can synchronously follow the magnet with 5 mT/mm magnetic gradient and achieve a moving speed of up to 150 mm/s. The solid machines behaved similarly under the driven magnet with 4 mT/mm magnetic gradient until the translation speed of the magnet exceeded 60 mm/s due to an inadequate magnetic force. Solid MPTMs also exhibit locomotion in the rotating mode. As shown in [Figure 3C](#), solid MPTMs achieved synchronous rotation motion of up to 1,500 rpm under an external rotating magnetic field with 1 mT strength. Under a weaker field of 0.8 mT strength, a similar rotation motion of up to 450 rpm is observed. However, as the driving speed increases, the resistance from the surface becomes stronger until it cannot be balanced by the magnetic force. This causes the MPTM to lose its ability to synchronize with the magnetic field. Due to its excellent mobility and controllability, the solid MPTM can move rapidly along a trajectory formed by the letters "SYSU" ([Figure 1D](#) and [Video S1](#)). However, similarly to the jumping tests, liquid MPTMs presented poor mobility when subjected to the same magnetic field, as shown in [Figures 3B](#) and [3C](#), respectively. The reason for this is that the embedded NdFeB microparticles within the liquid MPTM are highly mobile and so their magnetic

polarity is not fixed because of the ability of the particles to freely rotate and change their orientation. This leads to an inability to generate adequate magnetic force or torque under external magnetic fields. Moreover, the adhesion between liquid matrix and substrate also hinders liquid MPTMs from fast locomotion.

Using the AMF heating process, MPTMs can transition from a solid to liquid phase and exhibit morphological adaptability (i.e., deformability) such as controllable elongation, splitting, and merging enabled by the reconfigurable magnetic polarity of embedded NdFeB microparticles (Figures 3D–3F and Video S5). We first studied the ability of elongation by deforming a spherical MPTM droplet into an oval shape by applying a magnetic field gradient (i.e., moving a permanent magnet at one end of the droplet). Elongation is characterized by the maximum aspect ratio (ratio of the long axis and the short axis a/b , Figure 3D, inset) achieved by liquid MPTMs, as shown in Figure 3D. The maximum aspect ratio increases with the size of the droplet and can reach 27.5 mm with liquid MPTM droplets of 12 μL volume. The mechanism of elongation is that the suspended NdFeB microparticles accumulate at the ends of the liquid MPTM droplet and move along with the moving magnet to stretch the droplet. The surface tension of the LM matrix assists in the elongation by regulating the minimum width of the minor axis for different sizes of liquid MPTMs (e.g., 1.6 mm in the case of the droplet shown in Figure 3D).

Liquid MPTMs can also perform splitting by using two magnets. Instead of a single magnet applied at one end (as is used for elongation), two magnets at both ends are applied to continuously stretch the liquid MPTM and finally rupture the droplet at the middle to form two smaller droplets. This separation is induced by the Plateau-Rayleigh instability of the LM matrix,²⁹ as shown in the inset of Figure 3E. The number of smaller droplets that are formed depends on the size (i.e., total volume) of liquid MPTM (Figure 3E) because the minimum size of liquid MPTM for a successful split is regulated by the balance between the surface tension of the LM matrix and magnetic force provided by suspended NdFeB microparticles, which is 3 μL (Figure 3E). Two liquid MPTMs can also be attracted to each other and achieve on-demand merging using magnets, which will cause the oxide coating of the gallium matrix to rupture.⁵⁴ When the ruptured surfaces are in contact, the high surface tension of the liquid gallium will cause the droplets to coalesce (Figure S13 and Video S5).⁵⁵ Figure 3F shows that the magnetic polarity of liquid MPTM droplets can be altered by the applied external rotating magnetic field, caused by reorientation of the suspended NdFeB microparticles in the LM matrix.⁵⁶ The results show that the magnetic polarities of liquid MPTMs can be visualized using a magnetic display card (Figure 3F, inset), and the polar orientation of the liquid MPTM droplets are aligned with the external magnetic field. In summary, the results in Figures 3A–3F suggest that MPTMs exhibit an exceptional combination of multimodal locomotion capabilities and controllability (e.g., can achieve jumping, moving, and rotation with high speed in solid phase), morphological adaptability, and reconfigurability (e.g., can achieve elongation, splitting, and merging in liquid phase). The typical behaviors of MPTM and other LM-based materials are compared in Table S2.

Complex motions through phase change

We next conducted several representative demonstrations that highlight the critical role of solid-liquid phase transition for performing complex tasks (Figures 3G–3I and S14; Videos S6, S7, and S8). We demonstrate that MPTM can pass through a complex multi-terrain surface, including a deep moat, high wall, and grid surface, as shown in Figure 3G and Video S6. The width of the solid MPTM and the deep moat were 3 and 21 mm, respectively. In its solid phase, the MPTM was able to

jump over the moat through the application of a magnetic field gradient along the z axis and then melt into a liquid state through the application of an AMF. The height of the liquid MPTM and the wall were 1 and 12 mm, respectively. The liquid-phase MPTM was stretched to 14 mm by the gradient magnetic field along the x axis and transformed into solid MPTM by cooling naturally, then climbed over the wall via the rotating magnetic field parallel to the xz plane. The width and spacing of the grids were 2 and 8 mm. Solid MPTM passed through the grid surface via a magnetic field gradient along the x axis.

Figure 3H presents a cooperative task of object manipulation to demonstrate the splitting and merging ability of MPTM in the liquid phase and the ability to achieve controlled motion and support high load capacity in the solid phase. A liquid MPTM was split into two smaller ones, which then transitioned into the solid phase. These two solid MPTMs applied a torque to rotate a rod by 90° anticlockwise and then pushed the rod to move forward by 14 mm. Finally, these solid MPTMs transitioned back to the liquid phase and merged to form the original droplet. As another example, **Figure 3I** shows the assembly of modular MPTMs into an intact rod structure with reconfigured magnetic polarity. Multiple solid MPTMs were self-assembled in a head-to-tail configuration assisted with magnetic attraction between opposite magnetic poles. Solid-to-liquid phase transition helped the assembled part to form an intact rod and meanwhile the polarity was altered by 90°, as shown in **Figure 3I**. The whole part was cooled down to solid phase and performed spinning and moving like typical solid MPTM. We also characterized the supercooling effect of MPTM by measuring the cooling curves of MPTM and Ga using differential scanning calorimetry (DSC) (**Figure S15**). The DSC results show that the solidification point of the MPTM is 17.4°C, which is much higher than that of pure gallium (−14.5°C), due to the doping of NdFeB microparticles. The doped microparticles will act as nucleation centers, allowing LM crystals to grow along the surface of the particles, which suppresses the supercooling effect of MPTMs.

Applications of MPTM

Having demonstrated the multifunctional capabilities of MPTMs, we next examined the ability to manipulate objects through wireless operation in confined spaces. By leveraging the abilities mentioned above, we demonstrate the following three applications of MPTMs for use in confined spaces: electronics soldering, mechanical assembly, and a magnetic rotor.

Smart soldering machines for circuit assembly and repair

In addition to their wireless functionality and ability to undergo solid-liquid phase transition, MPTMs also exhibit metal-like electrical conductivity. Together, these properties enable MPTMs to be used as remotely operated soldering devices for electronics assembly and repair in confined spaces that are hard to reach (**Figure 4A** and **Video S9**). To demonstrate this, we remotely controlled MPTMs ($3 \times 3 \times 1 \text{ mm}^3$) as smart soldering machines to transport a light-emitting diode (LED) to a target spot in a circuit with external magnetic field (**Figure 4B**). Soldering machines wrapped the LED pins. Next, solid-to-liquid phase transition was performed in order to form electrical connections between the pins and soldering pads. Ambient cooling enabled the liquid to solid phase transition of MPTMs in order to complete the soldering of the LED pins and circuit pads (**Figure 4C**).^{57,58} After flipping the circuit board, the LED lamp remained firmly attached to the pad. Instead of magnetic LMs acting as conductive switches, MPTM can form stable mechanical connections between pads and electronic components because of its ability to support stress

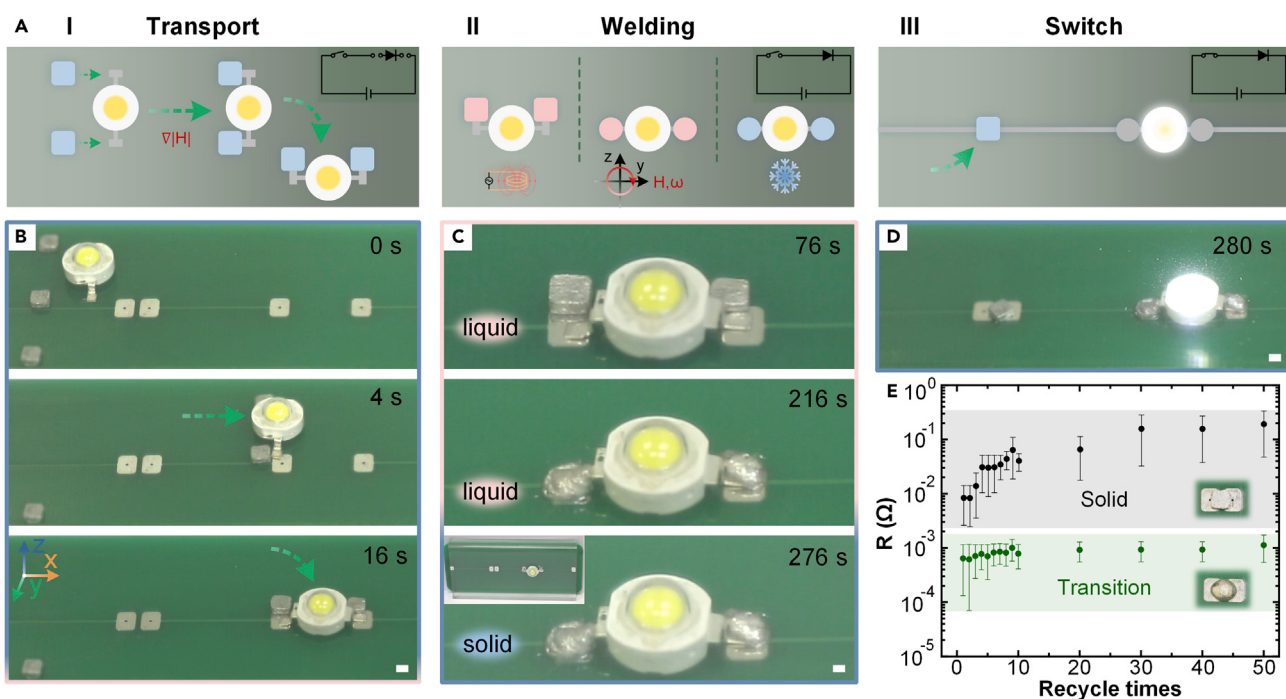


Figure 4. MPTMs as magnetic solder using a liquid-solid transition

- (A) Illustration of MPTMs assembling an LED light and connecting circuits in confined spaces.
- (B) Sequential optical images of MPTMs transporting LED light. Green arrows indicate translational and rotational motion directions of MPTMs.
- (C) Sequential optical images of the process of welding LED lights with MPTMs as magnetic solders.
- (D) Sequential optical images of MPTMs as switch connecting the circuit.
- (E) Resistance changes of MPTM and solid MPTM along recycle times.

All scale bars represent 2 mm.

when solidified (Figure 4C, inset). Following this process for each solder connection, we created a fully functional LED circuit (Figure 4D). We also characterized MPTMs as solder joints by measuring their contact resistance under repeated cycles of phase change between solid and liquid (Figure 4E). The contact resistance of the magnetic solder after phase transition is about $10^{-3} \Omega$, which is two orders of magnitude lower than that of a solid magnetic switch. We also evaluated the bonding force of MPTMs for circuit soldering. The results show appreciable bonding force of MPTMs (131 N), which is comparable with the bonding force of traditional solder (792 N) (Figure S16). This demonstration suggests that MPTM has the potential to perform circuit assembly and repair in a wireless manner.

Universal screws for smart assembly

The dislodgment and damage of loose screws often bring safety risks to the operation of precision hardware. Wireless operability and high load capacity in the solid phase and morphological adaptability in the liquid phase endow MPTMs with the potential to function as a “universal” mechanical screw for smart assembly and repair within confined or hard-to-reach spaces. We demonstrated this by setting up an application in which MPTMs are remotely operated to pass through a narrow space and function as a screw to join two plastic plates (Figures 5A and S17; Video S10). Two solid MPTMs ($6 \times 6 \times 2 \text{ mm}^3$) enter the confined space and move to the top of threaded holes (Figure 5B). AMF heating is then used to transform the MPTM into a liquid that then fills the threaded holes to form screws. Next, the MPTM solidifies under ambient cooling to form solid screws that join the plates together

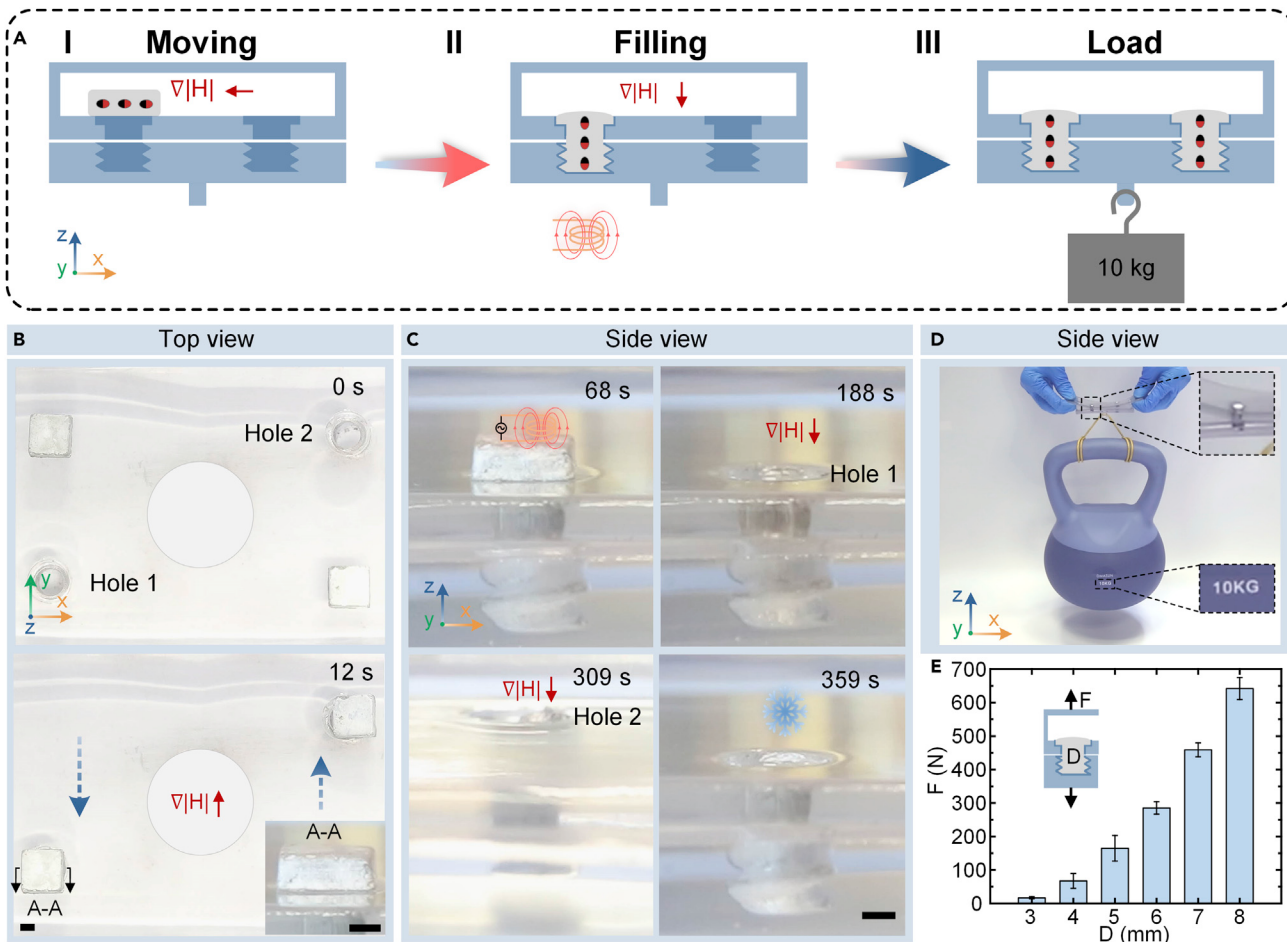


Figure 5. MPTMs as magnetic universal screws utilizing liquid-solid transition

(A) Schematic illustration of MPTMs filling threaded holes to connect polymer plates in confined spaces.

(B) Sequential optical images of the MPTM moving process. Blue arrows indicate translational motion directions of MPTMs. Scale bar, 2 mm.

(C) Sequential optical images of the process of MPTMs filling threaded holes. Scale bar, 2 mm.

(D) MPTM universal screws support 10 kg loading.

(E) Characterization of the load for different hole diameters.

(Figure 5C). This universal screw made of MPTM exhibits high load capacity as shown in Figure 5D, with a structure assembled with two MPTMs able to bear a load weighing 10 kg. We further quantified the load capacity of this universal screw as a function of the diameter of the threaded hole. The results shown in Figure 5E show that the universal screw can provide high load capacity (648 N at 9 mm diameter, $P > 14$ MPa). This demonstration highlights the morphological adaptability of liquid MPTMs to flow into mechanical joints and solidify to support structural integrity and high load capacity.

MPTMs for clearing of foreign body and drug delivery

To exhibit their potential use for *in vivo* biomedical applications, two representative demonstrations of MPTMs were performed with a human stomach model filled with water (Figure 6 and Video S11). Note that although the gallium was used for demonstrating the MPTM architecture, we can use other metals in order to tailor the melting point. For *in vivo* applications, such as phase transition in the human stomach, we can use gallium-based alloy ($\text{In}_{53}\text{Bi}_{25}\text{Sn}_{14}\text{Ga}_8$), which has a melting point of 45.6°C

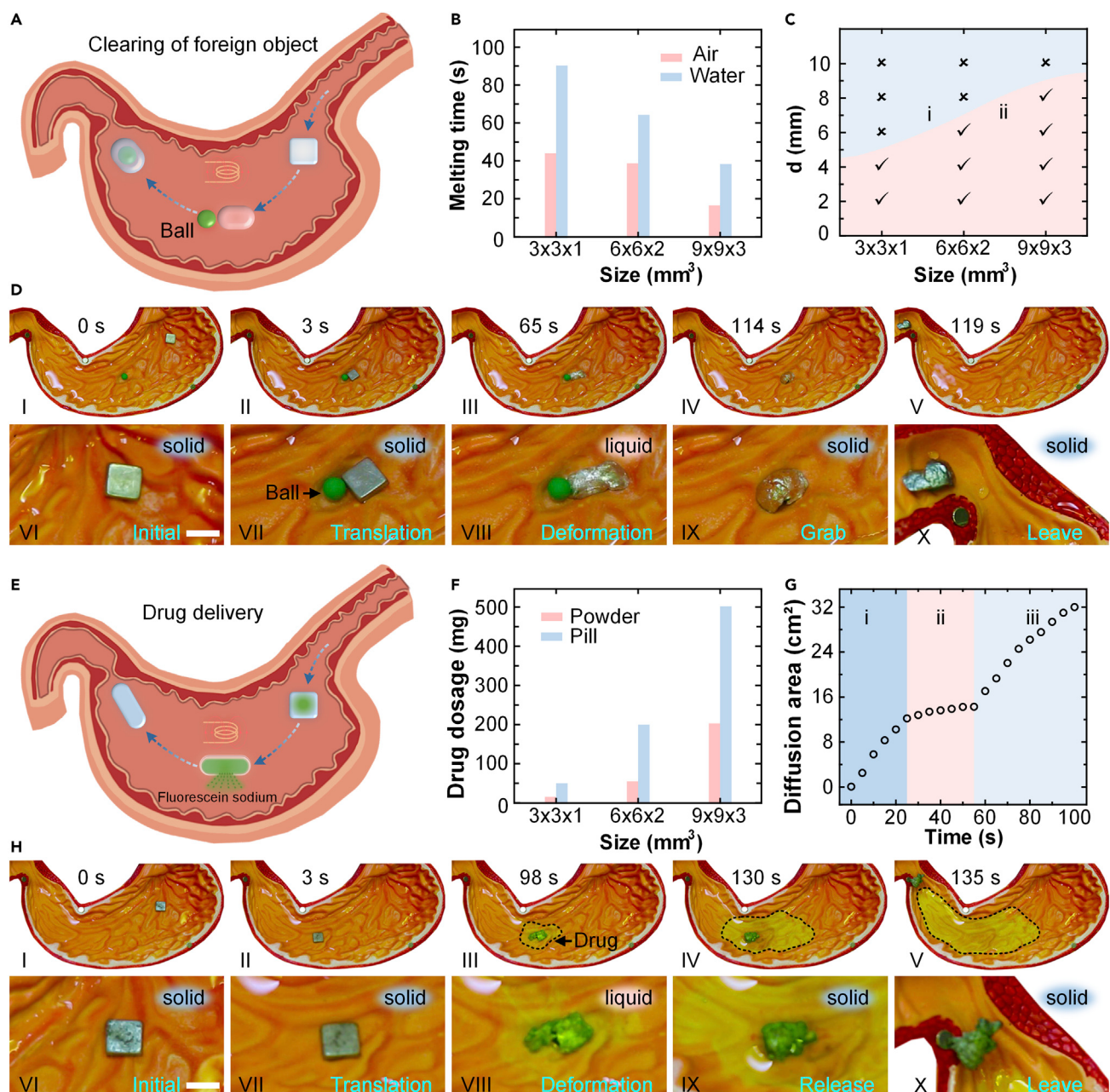


Figure 6. MPTMs clearing a foreign body and performing drug delivery

(A) Schematic illustration of MPTMs wrapped around a steel ball to remove it from the stomach. Blue arrows indicate translational motion directions of MPTMs.

(B) Characterization of melting time for MPTM of different sizes in air and water.

(C) Phase diagram reveals the grasp capability of MPTMs as a function of ball diameters and MPTM dimensions. Region (i) represents grasping failure while region (ii) represents grasping.

(D) Sequential optical images of the MPTM grasping process. Scale bar, 9 mm.

(E) Schematic illustration of MPTM capsule for drug delivery. Blue arrows indicate translational motion directions of MPTM.

(F) Characterization of drug-delivery dosage for MPTMs of different sizes.

(G) During the stomach-like structure drug-delivery process, the drug diffusion area increases with time. Region (i) represents the stretching process of the MPTM. Regions (ii) and (iii) represent MPTM rotating at 0 rpm and 60 rpm.

(H) Sequential optical images of the MPTM drug-delivery process. Scale bar, 9 mm.

(Figure S3B). This is greater than the temperature within the human stomach, which is expected to be in the range of 37.5°C–38°C. The first demonstration shows the ability to remove a foreign object from the stomach. In practice, such an object could cause gastrointestinal damage or even be life threatening. As the illustration shown in Figure 6A suggests, the solid MPTM can move quickly to the location of a foreign object (a ball), transition into the liquid phase and encompass the object, transition back to the solid phase, and remove the object from the stomach. Figure 6D presents snapshot images of key steps of this object removal process. The solid MPTM ($9 \times 9 \times 3 \text{ mm}^3$) moves quickly to the designated location within 3 s. MPTM is transitioned to liquid phase by AMF heating followed by the deformation of the machine to swallow the object (diameter of the ball is 6 mm) ($t = 65 \text{ s}$). The liquid MPTM is naturally cooled to the solid state to finish the grabbing operation ($t = 114 \text{ s}$). The object contained within the solid MPTM could also be removed from the stomach very quickly (within 5 s). We also investigated the influence of machine size and surrounding environment on the heating rate (Figure 6B). The results show that it takes longer to melt MPTMs in water than in air, due to the higher thermal conductivity of water. Smaller MPTMs take a longer time to melt because a greater proportion of heat will dissipate to the environment relative to the heat generated from AMF. The relationship between machine size and grasp capability (i.e., maximum object size that can be grasped) was also investigated, as shown in Figure 6C, where regions (i) and (ii) represent the failure and success of grasping, respectively. This demonstration suggests the MPTM has potential as a medical machine for non-invasive operations that require fast response time and a high degree of deformability.

The second biomedical demonstration involves the use of MPTM as a “smart” capsule to perform on-demand drug delivery. For this demonstration, we used fluorescein sodium as the model drug.⁵⁹ As the illustration in Figure 6E and Video S12 show, the solid MPTM capsule with the drug moves quickly to the stomach, transitions to the liquid phase and releases the drug, transitions back to the solid phase, and finally leaves the stomach after it has completed drug delivery. We investigated the influence of MPTM capsule size on the drug-delivery dosage (Figure 6F). The results show that larger MPTMs can carry more drugs. Figure 6H shows snapshot images of key moments of a typical on-demand drug-delivery process by MPTM. The drug-loaded (200 mg) solid MPTM ($9 \times 9 \times 3 \text{ mm}^3$) moved quickly toward the designated location within 3 s. No fluorescence leakage was observed at this stage. Following AMF heating and solid-to-liquid phase change, the capsule released the drug ($t = 98 \text{ s}$). After completing the drug release, the MPTM resolidified and was removed from the stomach. In the solid state, the MPTM can accelerate the drug diffusion by spinning and creating turbulence in the surrounding fluid. As shown in Figure 6G, the drug diffusion within the stomach was recorded: regions (i) to (iii) represent the drug release and diffusion by stretching the liquid MPTM for drug diffusion without spinning and with 60 rpm spinning, respectively. To find out whether the high-melting-point alloy could successfully release the drug, we used MPTM-46 instead of MPTM to perform the experiments in the stomach model. MPTM-46 consists of the high-melting-point alloy $\text{In}_{53}\text{Bi}_{25}\text{Sn}_{14}\text{Ga}_8$. The experimental results show that the MPTM-46 can be heated from 37°C to 46°C by AMF (Figure S18). Eventually, the MPTM-46 managed to release the drug (Video S13). This demonstration suggests that MPTM has the potential for on-demand cargo delivery in biomedical applications. Gallium below 700 mg/kg is considered safe and non-toxic *in vivo*, and gallium has strong metabolic capacity.⁶⁰ At present, there is still much work to be done on *in vivo* applications, such as programmable magnetic field control (Figure S19 and Video S14) and real-time imaging. Above

all, MPTMs exhibit the excellent adaptability of transformation and locomotion in both dry and wet environments in an untethered and controllable manner.

Conclusions

We have reported a magnetically actuated phase-changing material that is composed of NdFeB microparticles embedded within a matrix of low-melting-point LM. This material system can achieve high mechanical strength (tensile strength, 21.2 MPa; compressive strength, 18.8 MPa; stiffness, 1.98 GPa), high load capacity (capable of 30 kg load for a 6 mm universal screw), and fast and multimodal locomotion (jumping up to 20 times body length, moving up to 1.5 m/s, and rotating up to 1,500 rpm) in its solid state as well as excellent morphological adaptability (elongation, splitting, and merging) and reconfigurable magnetic polarity in its liquid state. This unique combination of properties is enabled by the reversible transition of MPTMs between rigid and fluidic states through AMF heating and ambient cooling. To illustrate the unique capabilities of MPTM, we demonstrate smart soldering machines that can manipulate and solder electronic components to create a functional circuit. We also use MPTMs as universal screws to assemble parts in hard-to-reach space and as a capsule machine for removing foreign objects or delivering drugs in a model stomach. The diverse unprecedented functionalities demonstrated by MPTMs are promising for future applications in flexible electronics, healthcare, and robotics that depend on dynamic shape reconfigurability and repair.

EXPERIMENTAL PROCEDURES

Resource availability

Lead contact

Further information and requests for resources and reagents should be directed to and will be fulfilled by the lead contact, Lelun Jiang (jianglel@mail.sysu.edu.cn).

Materials availability

This study did not generate new, unique reagents.

Data and code availability

The data presented in this work are available from the [lead contact](#) upon reasonable request. This study did not analyze code.

Preparation of MPTM

MPTM was prepared by mechanically mixing the NdFeB magnetic particles (average diameter: 38 μ m; Magnequench, China) with the pure gallium (purity of 99.9%; Dongguan ding Tai metal materials) using a mortar and pestle in air. Gallium remains liquid during the mixing process by heating at a temperature of \approx 35°C. The ratio of magnetic particles to pure gallium is 1:9. MPTMs were prepared by solidifying in polydimethylsiloxane (PDMS) (Sylgard 184; Dow Corning) molds of prefabricated shapes. MPTM was then magnetically saturated through a 3 T pulsed magnetic field from a magnetizer (MA-2030; Shenzhen Jiuju Industrial Equipment, China).

Characterization of MPTM

The morphology and elemental composition of MPTM were characterized via SEM (QUANTA 400F, Japan) and EDS, respectively. The solid-liquid behavior of MPTM was characterized by DSC (200F3Maia; NETZSCH). The temperature rise curves of MPTM under electromagnetic heating and cooling were obtained by an infrared camera (FLIR A65; Pumeng Technology). In the heating process, the frequency of AMF is 50 kHz. The hysteresis loop is obtained using a magnetic properties

measurement system (MPMS-VSM and MPMS-XL; Quantum Design). The dynamic viscosity of liquid MPTM samples was measured using a rotating parallel plate rheometer (DHR-2; Waters, USA). This was achieved by placing the sample in a 1-mm gap between the two plates of the rheometer and applying loads with shear rates ranging from 1 to 100 s⁻¹ at a constant test temperature of 50°C.

A dogbone-shaped specimen was fabricated for tensile testing, as shown in [Figure S6A](#). The original gauge length L_0 , cross-section width b , and thickness a of the specimen were 32, 4, and 2 mm, respectively. A cylindrical specimen with a diameter d of 6 mm and height L of 6 mm was manufactured for compression testing, as shown in [Figure S6B](#). Tensile and compression tests were carried out according to standard documents “GB/T 228.1-2010 Metallic materials—tensile testing at ambient temperature” and “GB/T 7314-2017 Metallic materials—compression test method at room temperature,” respectively. These mechanical tests were performed using a universal testing machine (LR10K Plus; Lloyd Instruments, Bognor Regis, UK) with a 1,000-N load cell. The tensile rate and compression rate were 0.03 mm s⁻¹. The experimental process was recorded with a digital camera (Canon 5e; Canon, China).

Liquid-solid phase transitional machine

The MPTM was wirelessly heated using a ZVS high-frequency induction heating device (HG-3KW; Qingdao Huguang Electronics). The ZVS high-frequency induction heater contained an alternating current generator connected to a copper plate coil, which is 5 cm thick and has a diameter of 7.5 cm and is connected to a water-cooling system. The heater was powered by a 48-V, 50-A constant voltage source (ZXD3000; ZTE, China).

For application of the magnetic field, permanent magnets (N45; Lalaci, Shenzhen) were used to generate the field, whereby the gradient magnetic field was generated by the 2 × 2 × 20 mm³ permanent magnet. The rotating magnetic field was generated by the 25 × 25 × 50 mm³ permanent magnet rotating on the motor.

Solid MPTM behaviors

The magnetic field gradient was adjusted by changing the distance of permanent magnets, and the jump height was measured by vernier calipers ([Figure 3A](#)). In motion and rotation ([Figures 3B and 3C](#)), different motion and rotation speeds of the magnets were obtained by adjusting the speed of the linear motor and the speed of the magnetic stirrer. The moving and rotating behaviors of MPTMs were captured using a high-speed camera (960 fps; FASTEC-TS3, China). The following speed was obtained by video processing.

Liquid MPTM behaviors

MPTMs of different sizes deformed under application of the magnetic field ([Figures 3D and 3E](#)). The deformability and the maximum splitting number were measured using vernier calipers. Surface magnetic field distribution of MPTMs was visualized using a magnetic display card ([Figure 3F](#)).

Smart soldering MPTM devices

The resistance of solid-state and phase-transitioning MPTM devices for soldering were measured using a multimeter ([Figure 4E](#)). The solid-state material contacted the pad and the resistance was measured. The cycle was repeated 50 times. The phase transitional devices melted into a liquid state, fully contacted the pad, and finally solidified into a solid state. The resistance was measured and cycled 50 times.

Universal screws

Parts with threaded holes of different diameters were 3D printed by the stereolithography technique using a commercial 3D printer (Form3; Formlabs). According to the thread standard "GB/T197-2018," models of M3 \times 0.8-S, M4 \times 0.8-S, M5 \times 0.8-S, M6 \times 1.5-S, M7 \times 1.5-S, and M8 \times 1.5-S threaded holes were manufactured (Figure 5E). The MPTM material filled the threaded holes and the maximum tension was measured using a universal testing machine with a 1,000-N load cell. The tensile rate was 0.03 mm s⁻¹.

Clearing of foreign body

MPTM materials of dimensions 3 \times 3 \times 1 mm³, 6 \times 6 \times 2 mm³, and 9 \times 9 \times 3 mm³ were manufactured using PDMS molds. To achieve phase transition, they were melted in air and water and heated by AMF. The time required for melting was recorded (Figure 6E). The maximum diameters of iron beads that could be securely wrapped by machines of different sizes were recorded (Figure 6C).

Drug delivery

The *in vitro* drug-delivery test of the MPTM was performed in a stomach-like structure filled with water (Figures 6F and 6G). Fluorescein sodium was used as a powder model drug, being mixed in sucrose in equal quantities. The mold was used to prepare sodium fluorescein into tablets. In the process of preparing MPTM, the tablets were placed in the middle of the LM with tweezers. Finally, the whole cooling and magnetization were used to successfully prepare MPTM loaded with drugs. The maximum drug dosage that could be hermetically encapsulated by the MPTM was recorded. The change of drug diffusion area over time in the drug administration experiment was recorded by analyzing Video S12.

Finite element analysis

The magnetic field generated by the permanent magnet was analyzed using FEA software COMSOL Multiphysics (Version 5.4; COMSOL, Sweden), and the magnetic field distribution was obtained, as shown in Figure S9. The FEA model of permanent magnets was three-dimensional and included the air domain (100 \times 100 \times 100 mm³) and magnets domain (25 \times 25 \times 50 mm³; 2 \times 20 \times 2 mm³). These domains were meshed with tetrahedral range of <1 mm and hexahedral range of 0.2 mm. The residual flux density model was employed as the magnetic constitutive relationship. The relative permeability and residual magnetic flux density of the permanent magnets was set as 1.05 T and 1.25 T. The magnetic field distribution of the permanent magnet was calculated.

SUPPLEMENTAL INFORMATION

Supplemental information can be found online at <https://doi.org/10.1016/j.matt.2022.12.003>.

ACKNOWLEDGMENTS

This research is financially supported by the National Natural Science Foundation of China (project no. 51975597, China), the Natural Science Foundation of Guangdong Province (project no. 2022B1515020011, China), and the Shenzhen Science and technology project (project no. JCYJ20220818102201003, China).

AUTHOR CONTRIBUTIONS

Q.W. and C.P. conceived the idea. Q.W., C.P., Y.Z., L.P., Z.C., C.M., and L.J. designed the research. Q.W., C.P., Y.Z., L.P., and Z.C. performed the experiments of complex motions through phase change. Q.W. and C.P. produced the

demonstrations of smart soldering machines for circuit assembly and repair, universal screws for smart assembly, and MPTMs for clearing of foreign body and drug delivery. Q.W., C.P., and Y.Z. demonstrated the robotic arm teleoperation. Q.W., C.P., C.M., and L.J. analyzed the experimental data and wrote the manuscript. L.J. and C.M. coordinated and supervised the research.

DECLARATION OF INTERESTS

The authors declare no competing interests.

Received: August 18, 2022

Revised: October 28, 2022

Accepted: December 5, 2022

Published: January 25, 2023

REFERENCES

1. Zhang, J., Ren, Z., Hu, W., Soon, R.H., Yasa, I.C., Liu, Z., and Sitti, M. (2021). Voxelated three-dimensional miniature magnetic soft machines via multimaterial heterogeneous assembly. *Sci. Robot.* 6, eabf012. <https://doi.org/10.1126/scirobotics.abf012>.
2. Zhao, X., Kim, J., Cezar, C.A., Huebsch, N., Lee, K., Bouhadir, K., and Mooney, D.J. (2011). Active scaffolds for on-demand drug and cell delivery. *Proc. Natl. Acad. Sci. USA* 108, 67–72. <https://doi.org/10.1073/pnas.1007862108>.
3. Yim, S., and Sitti, M. (2012). Design and rolling locomotion of a magnetically actuated soft capsule endoscope. *IEEE Trans. Robot.* 28, 183–194. <https://doi.org/10.1109/TRO.2011.2163861>.
4. Liu, X., Yang, Y., Inda, M.E., Lin, S., Wu, J., Kim, Y., Chen, X., Ma, D., Lu, T.K., and Zhao, X. (2021). Magnetic living hydrogels for intestinal localization, retention, and diagnosis. *Adv. Funct. Mater.* 31, 2010918. <https://doi.org/10.1002/adfm.202010918>.
5. Yu, W., Lin, H., Wang, Y., He, X., Chen, N., Sun, K., Lo, D., Cheng, B., Yeung, C., Tan, J., et al. (2020). A ferrobotic system for automated microfluidic logistics. *Sci. Robot.* 5, eaba4411. <https://doi.org/10.1126/scirobotics.aba4411>.
6. Zhang, J., Guo, R., and Liu, J. (2016). Self-propelled liquid metal motors steered by a magnetic or electrical field for drug delivery. *J. Mater. Chem. B* 4, 5349–5357. <https://doi.org/10.1039/c6tb00996d>.
7. Wang, Y., Duan, W., Zhou, C., Liu, Q., Gu, J., Ye, H., Li, M., Wang, W., and Ma, X. (2019). Phoretic liquid metal micro/nanomotors as intelligent filler for targeted microwelding. *Adv. Mater.* 31, e1905067. <https://doi.org/10.1002/adma.201905067>.
8. Kim, H., Lee, K., Oh, J.W., Kim, Y., Park, J.-E., Jang, J., Lee, S.W., Lee, S., Koo, C.M., and Park, C. (2022). Shape-Deformable and Locomotive MXene (Ti3C2Tx)-Encapsulated Magnetic Liquid Metal for 3D-Motion-Adaptive Synapses. *Adv. Funct. Mater.* 2210385. <https://doi.org/10.1002/adfm.202210385>
9. Boyvat, M., and Sitti, M. (2021). Remote modular electronics for wireless magnetic devices. *Adv. Sci.* 8, e2101198. <https://doi.org/10.1002/advs.202101198>.
10. Peng, L., Zhang, Y., Wang, J., Wang, Q., Zheng, G., Li, Y., Chen, Z., Chen, Y., Jiang, L., and Wong, C.-P. (2022). Slug-inspired magnetic soft millirobot fully integrated with triboelectric nanogenerator for on-board sensing and self-powered charging. *Nano Energy* 99, 107367. <https://doi.org/10.1016/j.nanoen.2022.107367>.
11. Zhou, M., Wu, Z., Zhao, Y., Yang, Q., Ling, W., Li, Y., Xu, H., Wang, C., and Huang, X. (2019). Droplets as carriers for flexible electronic devices. *Adv. Sci.* 6, 1901862. <https://doi.org/10.1002/advs.201901862>.
12. Chen, Y., Zhou, T., Li, Y., Zhu, L., Handschuh-Wang, S., Zhu, D., Zhou, X., Liu, Z., Gan, T., and Zhou, X. (2018). Robust fabrication of nonstick, noncorrosive, conductive graphene-coated liquid metal droplets for droplet-based, floating electrodes. *Adv. Funct. Mater.* 28, 1706277. <https://doi.org/10.1002/adfm.201706277>.
13. Kim, Y., and Zhao, X. (2022). Magnetic soft materials and robots. *Chem. Rev.* 122, 5317–5364. <https://doi.org/10.1021/acs.chemrev.1c00481>.
14. Hu, W., Lum, G.Z., Mastrangeli, M., and Sitti, M. (2018). Small-scale soft-bodied robot with multimodal locomotion. *Nature* 554, 81–85. <https://doi.org/10.1038/nature25443>.
15. Xia, N., Jin, B., Jin, D., Yang, Z., Pan, C., Wang, Q., Ji, F., Iacovacci, V., Majidi, C., Ding, Y., and Zhang, L. (2022). Decoupling and reprogramming the wiggling motion of midge larvae using a soft robotic platform. *Adv. Mater.* 34, e2109126. <https://doi.org/10.1002/adma.202109126>.
16. Zhang, Y., Wang, Q., Yi, S., Lin, Z., Wang, C., Chen, Z., and Jiang, L. (2021). 4D printing of magnetoactive soft materials for on-demand magnetic actuation transformation. *ACS Appl. Mater. Interfaces* 13, 4174–4184. <https://doi.org/10.1021/acsami.0c19280>.
17. Xu, T., Zhang, J., Salehizadeh, M., Onaizah, O., and Diller, E. (2019). Millimeter-scale flexible robots with programmable three-dimensional magnetization and motions. *Sci. Robot.* 4, eaav4494. <https://doi.org/10.1126/scirobotics.aav4494>.
18. Kim, Y., Yuk, H., Zhao, R., Chester, S.A., and Zhao, X. (2018). Printing ferromagnetic domains for untethered fast-transforming soft materials. *Nature* 558, 274–279. <https://doi.org/10.1038/s41586-018-0185-0>.
19. Chen, W., Sun, M., Fan, X., and Xie, H. (2020). Magnetic/pH-sensitive double-layer microrobots for drug delivery and sustained release. *Appl. Mater. Today* 19, 100583. <https://doi.org/10.1016/j.apmt.2020.100583>.
20. Chen, W., Chen, X., Yang, M., Li, S., Fan, X., Zhang, H., and Xie, H. (2021). Triple-configurational magnetic robot for targeted drug delivery and sustained release. *ACS Appl. Mater. Interfaces* 13, 45315–45324. <https://doi.org/10.1021/acsami.1c14610>.
21. Zhu, J., Zhou, C., and Zhang, M. (2021). Recent progress in flexible tactile sensor systems: from design to application. *Soft Sci.* 1, 3. <https://doi.org/10.20517/ss.2021.02>.
22. Zhang, Q., Shi, Y., and Zhao, Z. (2021). A brief review of mechanical designs for additive manufactured soft materials. *Soft Sci.* 2, 2. <https://doi.org/10.20517/ss.2021.22>.
23. Wong, T.H., Yiu, C.K., Zhou, J., Song, Z., Liu, Y., Zhao, L., Yao, K., Park, W., Yoo, W., Song, E., et al. (2021). Tattoo-like epidermal electronics as skin sensors for human machine interfaces. *Soft Sci.* 1, 10. <https://doi.org/10.20517/ss.2021.09>.
24. Li, Y., Wang, P., Meng, C., Chen, W., Zhang, L., and Guo, S. (2021). A brief review on miniature flexible and soft tactile sensors for interventional catheter applications. *Soft Sci.* 2, 6. <https://doi.org/10.20517/ss.2022.05>.
25. Wang, B., Chan, K.F., Yuan, K., Wang, Q., Xia, X., Yang, L., Ko, H., Wang, Y.-X.J., Sung, J.J.Y., Chiu, P.W.Y., and Zhang, L. (2021). Endoscopy-assisted magnetic navigation of biohybrid soft microrobots with rapid endoluminal delivery and imaging. *Sci. Robot.* 6, eabd2813. <https://doi.org/10.1126/scirobotics.abd2813>.
26. Zhang, Y., Jiang, S., Hu, Y., Wu, T., Zhang, Y., Li, H., Li, A., Zhang, Y., Wu, H., Ding, Y., et al. (2022). Reconfigurable magnetic liquid metal robot for high-performance droplet manipulation. *Nano Lett.* 22, 2923–2933. <https://doi.org/10.1021/acs.nanolett.2c00100>.

27. Sun, M., Tian, C., Mao, L., Meng, X., Shen, X., Hao, B., Wang, X., Xie, H., and Zhang, L. (2022). Reconfigurable magnetic slime robot: deformation, adaptability, and multifunction. *Adv. Funct. Mater.* 32, 2112508. <https://doi.org/10.1002/adfm.202112508>.

28. He, X., Ni, M., Wu, J., Xuan, S., and Gong, X. (2021). Hard-magnetic liquid metal droplets with excellent magnetic field dependent mobility and elasticity. *J. Mater. Sci. Technol.* 92, 60–68. <https://doi.org/10.1016/j.jmst.2021.04.004>.

29. Li, X., Li, S., Lu, Y., Liu, M., Li, F., Yang, H., Tang, S.Y., Zhang, S., Li, W., and Sun, L. (2020). Programmable digital liquid metal droplets in reconfigurable magnetic fields. *ACS Appl. Mater. Interfaces* 12, 37670–37679. <https://doi.org/10.1021/acsami.0c08179>.

30. Li, F., Shu, J., Zhang, L., Yang, N., Xie, J., Li, X., Cheng, L., Kuang, S., Tang, S.-Y., Zhang, S., et al. (2020). Liquid metal droplet robot. *Appl. Mater. Today* 19, 100597. <https://doi.org/10.1016/j.apmt.2020.100597>.

31. Shu, J., Tang, S.Y., Feng, Z., Li, W., Li, X., and Zhang, S. (2018). Unconventional locomotion of liquid metal droplets driven by magnetic fields. *Soft Matter* 14, 7113–7118. <https://doi.org/10.1039/C8SM01281D>.

32. Fan, X., Dong, X., Karacakol, A.C., Xie, H., and Sitti, M. (2020). Reconfigurable multifunctional ferrofluid droplet robots. *Proc. Natl. Acad. Sci. USA* 117, 27916–27926. <https://doi.org/10.1073/pnas.2016388117>.

33. Jeong, J., Lee, J.-B., Chung, S.K., and Kim, D. (2016). Electromagnetic three dimensional liquid metal manipulation. *Lab Chip* 19, 3261–3267. <https://doi.org/10.1039/C9LC00503J>.

34. Jeon, J., Lee, J.-B., Chung, S.K., and Kim, D. (2016). Magnetic liquid metal marble: characterization of lyophobicity and magnetic manipulation for switching applications. *J. Microelectromech. Syst.* 25, 1050–1057. <https://doi.org/10.1109/JMEMS.2016.2614303>.

35. Li, F., Kuang, S., Li, X., Shu, J., Li, W., Tang, S.-Y., and Zhang, S. (2019). Magnetically- and electrically-controllable functional liquid metal droplets. *Adv. Mater. Technol.* 4, 1800694. <https://doi.org/10.1002/admt.201800694>.

36. Liu, M., Wang, Y., Kuai, Y., Cong, J., Xu, Y., Piao, H.G., Pan, L., and Liu, Y. (2019). Magnetically powered shape-transformable liquid metal micromotors. *Small* 15, e1905446. <https://doi.org/10.1002/smll.201905446>.

37. Fan, X., Sun, M., Sun, L., and Xie, H. (2020). Ferrofluid droplets as liquid microrobots with multiple deformabilities. *Adv. Funct. Mater.* 30, 2000138. <https://doi.org/10.1002/adfm.202000138>.

38. Xie, H., Sun, M., Fan, X., Lin, Z., Chen, W., Wang, L., Dong, L., and He, Q. (2019). Reconfigurable magnetic microrobot swarm: multimode transformation, locomotion, and manipulation. *Sci. Robot.* 4, eaav8006. <https://doi.org/10.1126/scirobotics.aav8006>.

39. Sun, M., Fan, X., Tian, C., Yang, M., Sun, L., and Xie, H. (2021). Swarming microdroplets to a dexterous micromanipulator. *Adv. Funct. Mater.* 31, 2011193. <https://doi.org/10.1002/adfm.202011193>.

40. Majidi, C. (2021). Fluid-like soft machines with liquid metal. *Matter* 4, 336–337. <https://doi.org/10.1016/j.matt.2021.01.009>.

41. Zhao, D., Pang, B., Zhu, Y., Cheng, W., Cao, K., Ye, D., Si, C., Xu, G., Chen, C., and Yu, H. (2021). A stiffness-switchable, biomimetic smart material enabled by supramolecular reconfiguration. *Adv. Mater.* 34, e2107857. <https://doi.org/10.1002/adma.202107857>.

42. Kennedy, E.B.L., Buresch, K.C., Boinapally, P., and Hanlon, R.T. (2020). Octopus arms exhibit exceptional flexibility. *Sci. Rep.* 10, 20872. <https://doi.org/10.1038/s41598-020-77873-7>.

43. Di Clemente, A., Maiole, F., Bornia, I., and Zullo, L. (2021). Beyond muscles: role of intramuscular connective tissue elasticity and passive stiffness in octopus arm muscle function. *J. Exp. Biol.* 224, 242644. <https://doi.org/10.1242/jeb.242644>.

44. Deng, H., Sattari, K., Xie, Y., Liao, P., Yan, Z., and Lin, J. (2020). Laser reprogramming magnetic anisotropy in soft composites for reconfigurable 3D shaping. *Nat. Commun.* 11, 6325. <https://doi.org/10.1038/s41467-020-2022-6>.

45. Song, H., Lee, H., Lee, J., Choe, J.K., Lee, S., Yi, J.Y., Park, S., Yoo, J.W., Kwon, M.S., and Kim, J. (2020). Reprogrammable ferromagnetic domains for reconfigurable soft magnetic actuators. *Nano Lett.* 20, 5185–5192. <https://doi.org/10.1021/acs.nanolett.0c01418>.

46. Ma, C., Wu, S., Ze, Q., Kuang, X., Zhang, R., Qi, H.J., and Zhao, R. (2020). Magnetic multimaterial printing for multimodal shape transformation with tunable properties and shiftable mechanical behaviors. *ACS Appl. Mater. Interfaces* 13, 12639–12648. <https://doi.org/10.1021/acsami.0c13863>.

47. Mattmann, M., De Marco, C., Briatico, F., Tagliabue, S., Colusso, A., Chen, X.Z., Lussi, J., Chautems, C., Pané, S., and Nelson, B. (2022). Thermoset shape memory polymer variable stiffness 4D robotic catheters. *Adv. Sci.* 9, e2103277. <https://doi.org/10.1002/advs.202103277>.

48. Testa, P., Style, R.W., Cui, J., Donnelly, C., Borisova, E., Derlet, P.M., Dufresne, E.R., and Heyderman, L.J. (2019). Magnetically addressable shape-memory and stiffening in a composite elastomer. *Adv. Mater.* 31, e190561. <https://doi.org/10.1002/adma.20190561>.

49. Lu, Y., Yu, D., Dong, H., Lv, J., Wang, L., Zhou, H., Li, Z., Liu, J., and He, Z. (2022). Magnetically tightened form-stable phase change materials with modular assembly and geometric conformativity features. *Nat. Commun.* 13, 1397. <https://doi.org/10.1038/s41467-022-29090-1>.

50. Zhou, X., Shu, J., Jin, H., Ren, H., Ma, G., Gong, N., Ge, D.-a., Shi, J., Tang, S.-Y., Yun, G., et al. (2022). Variable stiffness wires based on magnetorheological liquid metals. *Int. J. Smart Nano Mater.* 13, 232–243. <https://doi.org/10.1080/19475411.2022.2065703>.

51. Kalantar-Zadeh, K. (2020). Anisotropic materials based on liquid metals. *Matter* 3, 613–614. <https://doi.org/10.1016/j.matt.2020.08.015>.

52. Chen, S., Wang, H.-Z., Zhao, R.-Q., Rao, W., and Liu, J. (2020). Liquid metal composites. *Matter* 2, 1446–1480. <https://doi.org/10.1016/j.matt.2020.03.016>.

53. Ge, H., Li, H., Mei, S., and Liu, J. (2013). Low melting point liquid metal as a new class of phase change material: an emerging Frontier in energy area. *Renew. Sustain. Energy Rev.* 21, 331–346. <https://doi.org/10.1016/j.rser.2013.01.008>.

54. Zhou, Y.X., Zu, J.-S., and Liu, J. (2021). Insights into fluidic endogenous magnetism and magnetic monopoles from a liquid metal droplet machine. *Soft Sci.* 1, 15. <https://doi.org/10.20517/ss.2021.16>.

55. Ding, Y., Zeng, M., and Fu, L. (2020). Surface chemistry of gallium-based liquid metals. *Matter* 3, 1477–1506. <https://doi.org/10.1016/j.matt.2020.08.012>.

56. Cao, L., Yu, D., Xia, Z., Wan, H., Liu, C., Yin, T., and He, Z. (2020). Ferromagnetic liquid metal putty-like material with transformed shape and reconfigurable polarity. *Adv. Mater.* 32, e2000827. <https://doi.org/10.1002/adma.202000827>.

57. Wang, H., Chen, S., Li, H., Chen, X., Cheng, J., Shao, Y., Zhang, C., Zhang, J., Fan, L., Chang, H., et al. (2021). A liquid gripper based on phase transitional metallic ferrofluid. *Adv. Funct. Mater.* 31, 2100274. <https://doi.org/10.1002/adfm.202100274>.

58. Wang, H., Chen, S., Zhu, X., Yuan, B., Sun, X., Zhang, J., Yang, X., Wei, Y., and Liu, J. (2022). Phase transition science and engineering of gallium-based liquid metal. *Matter* 5, 2054–2085. <https://doi.org/10.1016/j.matt.2022.05.031>.

59. Chen, Z., Lin, Y., Zheng, G., Yang, Y., Zhang, Y., Zheng, S., Li, J., Li, J., Ren, L., and Jiang, L. (2020). Programmable transformation and controllable locomotion of magnetoactive soft materials with 3D-patterned magnetization. *ACS Appl. Mater. Interfaces* 12, 58179–58190. <https://doi.org/10.1021/acsami.0c15406>.

60. Wang, X., Li, X., Duan, M., Shan, S., Zhu, X., Chai, Y., Wang, H., Sun, X., Sheng, L., Qing, G., et al. (2022). Endosomal escapable cryo-treatment-driven membrane-encapsulated Ga liquid-metal transformer to facilitate intracellular therapy. *Matter* 5, 219–236. <https://doi.org/10.1016/j.matt.2021.11.006>.

Supplemental information

**Magnetoactive liquid-solid
phase transitional matter**

Qingyuan Wang, Chengfeng Pan, Yuanxi Zhang, Lelun Peng, Zhipeng Chen, Carmel Majidi, and Lelun Jiang

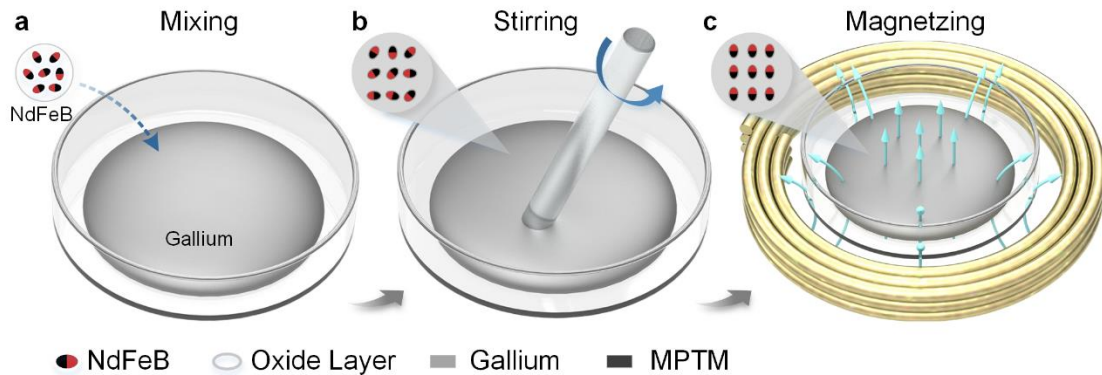


Figure S1. Schematic of MPTM preparation.

MPTM was prepared by mechanically mixing NdFeB magnetic particles with the pure gallium using a mortar and pestle in air. MPTM was then magnetically saturated through 3 T pulsed magnetic field from a magnetizer, as shown in the Figure S1. In the solid phase, the robots exhibit excellent mechanical integrity (stiffness: 1.98 GPa). This work demonstrates modulus changes of nearly four orders of magnitude, far larger than most stiffness-tuning matter prepared with phase change materials.

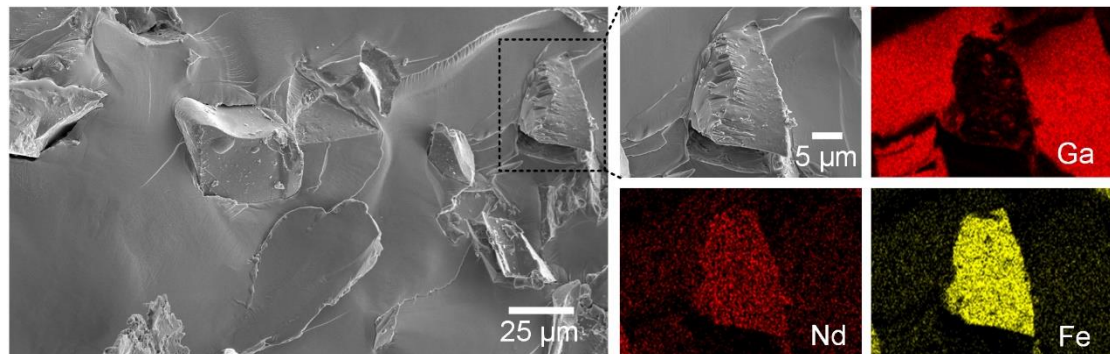


Figure S2. SEM and EDS mapping of MPTM.

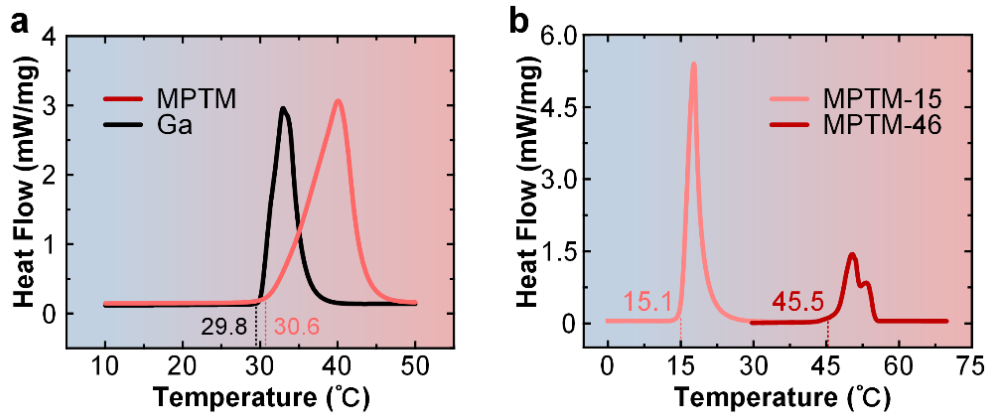


Figure S3. Comparison of thermal behavior between MPTM and Ga. (a) The melting curves of MPTM and Ga using differential scanning calorimetry (DSC). (b) The melting curves of MPTM-15 and MPTM-46 using differential scanning calorimetry (DSC). MPTM-15 and MPTM-46 are based on EGaIn ($\text{Ga}_{75}\text{In}_{25}$) and gallium-base alloy ($\text{In}_{53}\text{Bi}_{25}\text{Sn}_{14}\text{Ga}_8$), respectively.

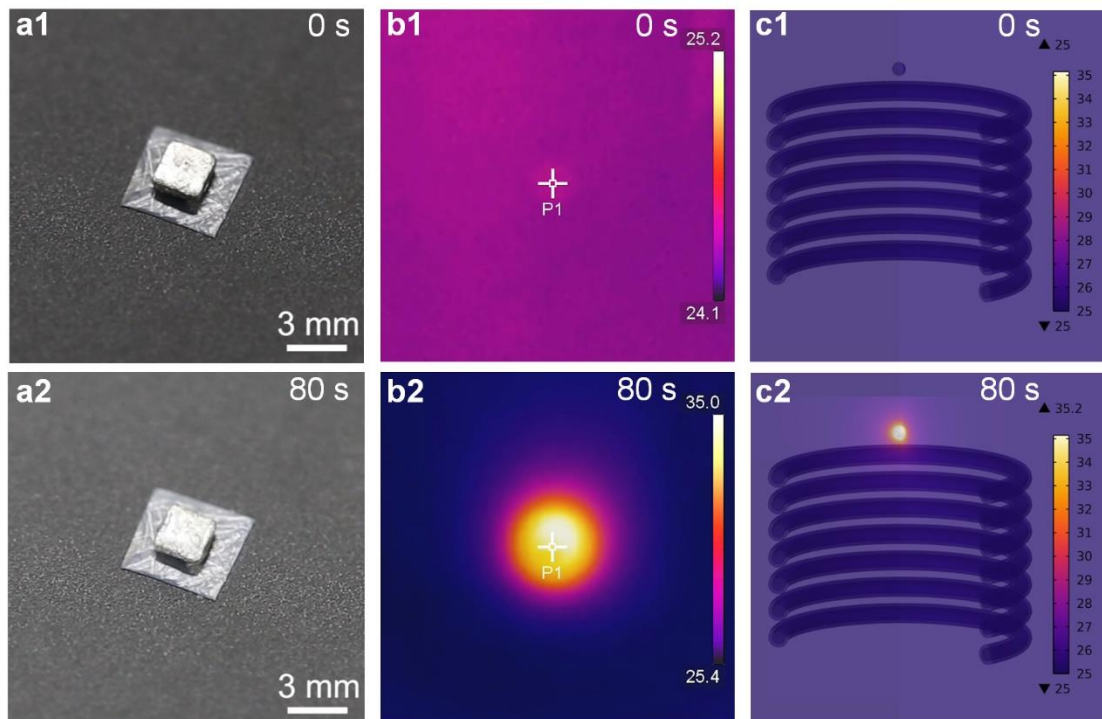


Figure S4. Infra-red images and simulated results of MPTM with AMF heating and air cooling. (a) Optical images and (b) infra-red images show the temperature change of MPTM with the heating by AMF. (c) Simulated heating results of MPTM.

As shown in Figure S4a-b, optical images and infra-red images show the temperature change of MPTM with the heating by AMF for a period of 80 s. Figure S4b showed the simulated heating results of MPTM with AMF.

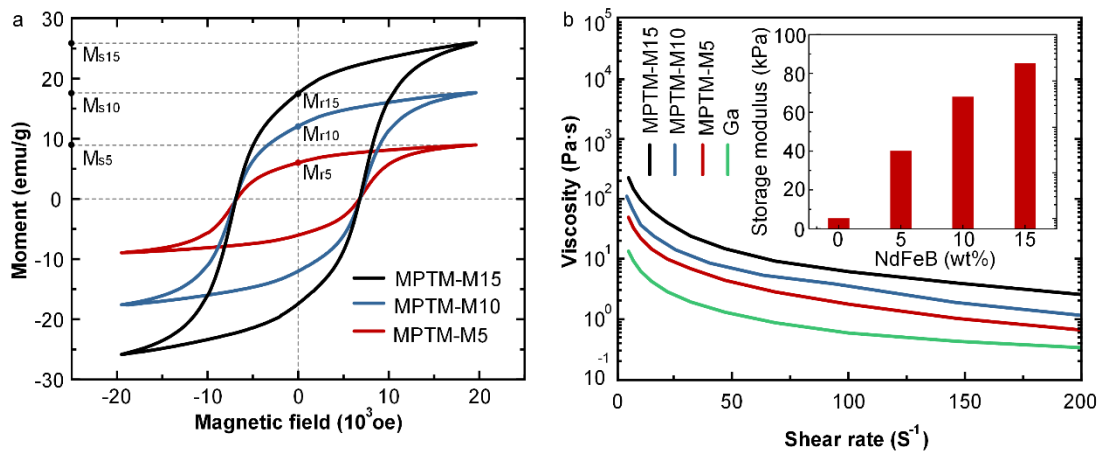


Figure S5. Properties of MPTM with different magnetic particle content. (a) Magnetization hysteresis loops of MPTM under different weight fraction of NdFeB microparticles. (b) The impacts of NdFeB microparticles on the viscosity of MPTM under different shear rates and storage modulus (inset).

Magnetic hysteresis loops were measured for the MPTM at room temperature (25 °C), as displayed in Figure S5a, showing the saturated magnetization value and remnant magnetization increasing through adding the NdFeB microparticles. We first study the rheological properties of liquid-phase MPTM by measuring its viscosity at different shear rates. The results in Figure S5b show that the viscosity increasing through adding the NdFeB microparticles. Furthermore, the amplitude sweep-based oscillatory tests were conducted to characterize the viscoelastic behavior of the MPTM samples. The storage modulus of the MPTM versus the fraction of NdFeB microparticles under a constant low strain amplitude (0.1%) and a constant frequency ($f = 1$ Hz) were presented in Figure S5b. The storage modulus has remarkable enhancement with increasing the fraction of the NdFeB microparticles.

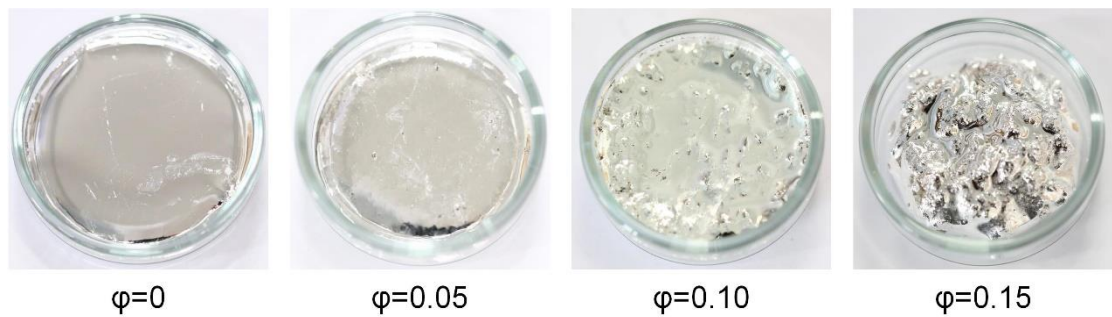


Figure S6. Photographs of MPTM samples in liquid phase with different packing ratio of NdFeB.

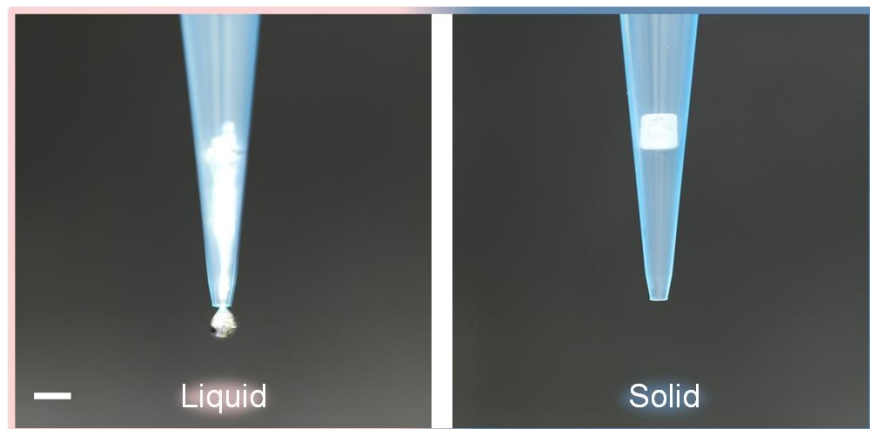


Figure S7. Photographs of MPTM in pipette with liquid and solid phase showing the morphological adaptability of liquid MPTM. Photos showing that liquid MPTM can flow out of the pipette tip (left), but solid MPTM can't (right). Scale bars, 3 mm.

Table S1. Maximum effective modulus and modulus ratio of MPTM and traditional machine.

Induction Method	Material Type		Maximum effective modulus (MPa)	Modulus ratio
Thermal	Magnetoactive Transitional Matter (MPTM)	Phase	1.98×10^3	2.9×10^4
Thermal	Shape memory polymers (SMP) ¹		1.48×10^3	1.48×10^2
Thermal	Conductive elastomer (CTPE) ²	Thermoplastic	10.4	14.8
Thermal	Thermoplastics (TP) ³		510	300
Pressure	Fluid-polymer (FPC) ⁴	composites	1.8×10^3	55
Pressure	Granular materials (GM) ⁵		110	50
Electric field	Electrorheological fluids (ERF) ⁶		0.075	6000
Electric field	Electroactive gel (EG) ⁷		0.25	13
Electric field	conductive propylene-based elastomer (CPBE) ⁸		175	83
Magnetic field	Magnetorheological fluid (MRF) ⁹		0.07	206
Magnetic field	Magnetorheological elastomers (MRE) ¹⁰		0.169	1.75

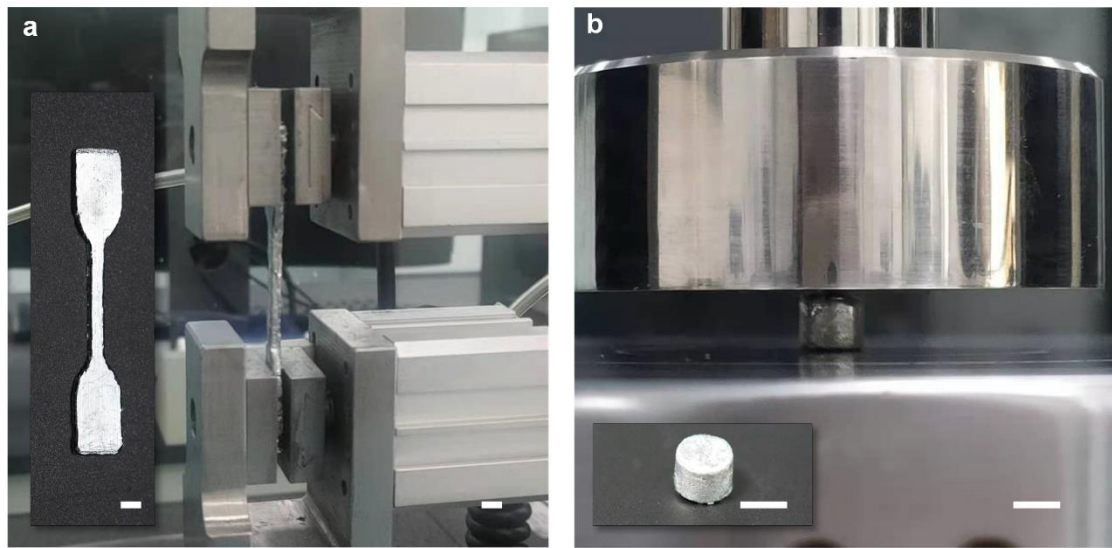


Figure S8. MPTM specimens for mechanical testing. (a) A dog bone-shaped specimen for tensile testing. (b) A cylindrical specimen for compression testing. Scale bar, 5 mm.

A specimen in dog bone-shaped was fabricated for tensile testing, as showing Figure S8a. The original gauge length L_0 , cross section width b and thickness a of specimen are 32 mm, 4 mm, and 2 mm, respectively. A cylindrical specimen with a diameter d of 6 mm and height L of 6 mm was manufactured for compression testing, as shown in Figure S8b. Tensile and compression tests were carried out according to standard documents “GB/T 228.1-2010 Metallic materials – Tensile testing at ambient temperature” and “GB/T 7314-2017 Metallic materials—Compression test method at room temperature” respectively.

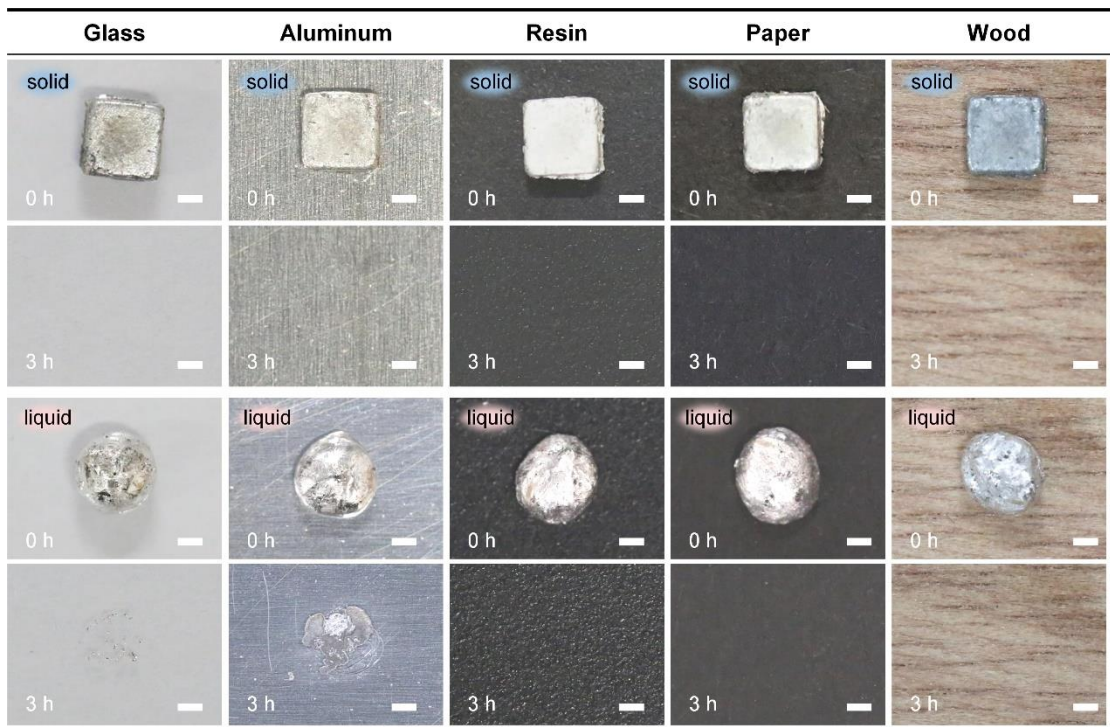


Figure S9. Behavior of MPTMs on various surfaces. Such as glass, aluminum, resin, paper, and wood. Surface residues was photographed 3 hours after place. Scale bars, 1 mm.

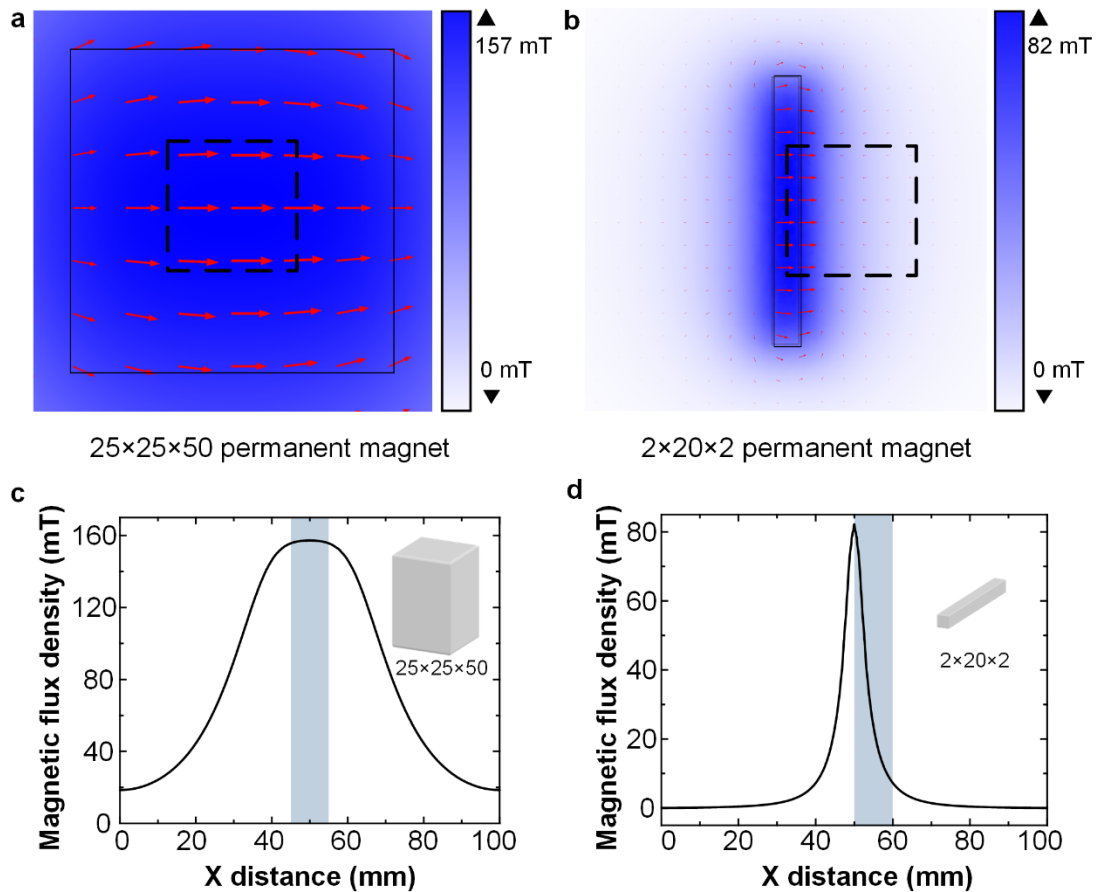


Figure S10. Simulation results of rotating magnetic field and gradient magnetic field. a) Simulation results of rotating magnetic field using a $25 \times 25 \times 50 \text{ mm}^3$ permanent magnet with a height of 10 mm. Magnetic field intensity (color maps) and force (red arrows). b) Simulation results of gradient magnetic field by $2 \times 20 \times 2 \text{ mm}^3$ permanent magnet with a height of 2 mm. c) The surface magnetic field distributions of $25 \times 25 \times 50 \text{ mm}^3$ permanent magnet along the x direction with a height of 10 mm. d) The surface magnetic field distributions of $2 \times 20 \times 2 \text{ mm}^3$ permanent magnet along the x direction with a height of 2 mm.

Figure S10a show that the magnetic field produced by the $25 \times 25 \times 50 \text{ mm}^3$ permanent magnet is evenly distributed in the working area. Since the magnetic field inhomogeneity ($\varepsilon = \frac{B_{\max} - B_{\min}}{B_0}$) is 0.8%, it was approximately uniform magnetic field, as shown in the Figure S10c. As the permanent magnet rotated, it created a rotating magnetic field. As shown in the Figure S10b and Figure S10d, the magnetic field produced by the $2 \times 20 \times 2 \text{ mm}^3$ permanent magnet has a gradient distribution along the x direction. The permanent magnets generated a gradient magnetic field to move the MPTM.

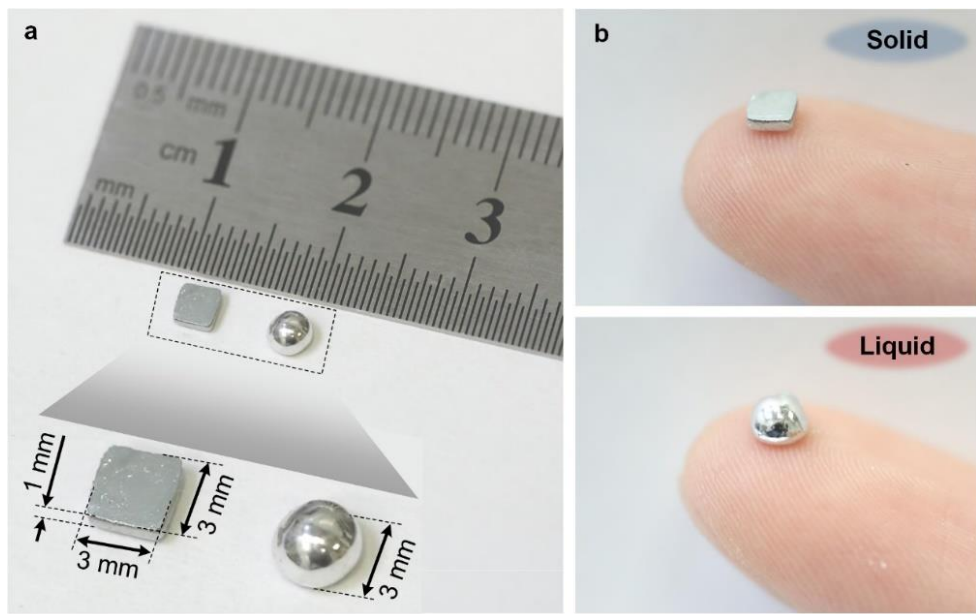


Figure S11. Top and side-view images of a solid MPTM and a liquid MPTM. a) top view images of a solid MPTM and a liquid MPTM. b) side-view images of a solid MPTM and a liquid MPTM on the fingertips.

Solid MPTM and liquid MPTM were manufactured by the template method and its dimensions are marked, as shown in the Figure S11a. The Gauge length, cross section length and width of solid MPTM are 25 mm, 4 mm, and 2 mm, respectively. A liquid MPTM of the same weight has a diameter of 3mm. Solid MPTM and liquid MPTM is placed on the fingertips, as shown in the Figure S11b.

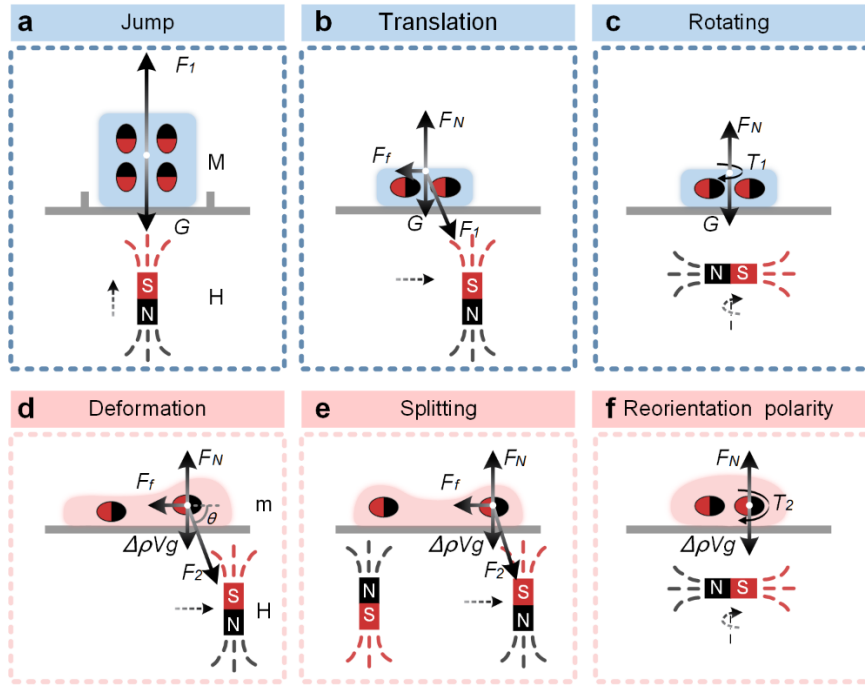


Figure S12. Typical magnetically actuated behaviors of solid and liquid MPTMs. a) jump, b) translation, c) rotating, d) deformation, e) splitting and f) reorientation polarity.

Solid MPTM can be regarded as a rigid body due to its high strength and stiffness. Under the gradient magnetic field \mathbf{H} , the solid MPTM was driven in the direction of the gradient of the field by magnetic force $F_1 = \mathbf{M} \cdot \nabla \mathbf{H} \cos(\theta)$ and gravity force G , where \mathbf{M} is remnant magnetization, θ denotes the angle between the horizontal direction and that of the applied magnetic field, respectively. $F_1 > G$ (Figure S12a). Solid MPTM could translate in the horizontal direction (Figure S12b) with magnetic force F_1 and sliding friction force F_f , $F > F_f$. The interaction between the residual magnetic field \mathbf{M} of the and the applied magnetic field of \mathbf{H} would generate a magnetic torque of $T_1 = \mathbf{M} \cdot \mathbf{H} \sin(\alpha)$, α denotes the angle between the direction of the remnant field and that of the applied magnetic field. The magnetic torque tended to realign the direction of the remnant field with the applied magnetic field (Figure S12c).

In its liquid phase, magnetic particles within the melted metal are driven directly by magnetic fields. Under the gradient magnetic field \mathbf{H} , liquid MPTM is driven in the direction of the gradient of the field by magnetic force $F_2 = \mathbf{m} \cdot \nabla \mathbf{H} \cos(\theta)$ along with the combined force of gravity and buoyancy $\Delta\rho Vg$, support force F_N and resistance force F_f , where $\Delta\rho$ is the density difference between gallium and the microparticles, \mathbf{V} is the volume of the microparticles, and g is the acceleration of gravity. (Figure S12d-e). The magnetic force caused magnetic particles to move in the direction of the gradient of the field. In the deformation and splitting process of liquid MPTM, magnetic particles suspended in the LM matrix may be accumulated at the ends to stretch the droplets. The interaction between the magnetized microparticles and the applied rotating magnetic field of \mathbf{H} would generate a magnetic torque of $T_2 = \mathbf{m} \cdot \mathbf{H} \sin(\alpha)$, where α denotes the angle between the direction of the remnant field and that of the applied magnetic field. The magnetic moment tended to realign the direction of \mathbf{m} with \mathbf{H} (Figure S13f).



Figure S13. Two liquid MPTMs achieve on-demand merging.

Table S2. Typical behaviors of MPTM and other LM based materials.

Ref(s).	Material(s)	Typical behaviors	Merits	Limits
Zhang et al ¹¹	Galinstan doped with Fe particles	droplet manipulation, splitting and merging	high-performance droplet manipulation	limited on superhydrophobic substrate
Li et al ¹²	Galinstan doped with Fe particles	transportation, deformation, splitting and merging	programmable digital control	limited on NaOH solution
He et al ¹³	Galinstan doped NdFeB particles	move in the microfluidic channel	excellent elasticity	low active deformability
Wang et al ¹⁴	Ga doped with Fe particles	magnetic grasp and connect electrical circuits	switchable adhesion force to arbitrarily shaped objects	phase change time consuming
This work	Ga doped with NdFeB particles	Jump, translation, rotating, deformation, splitting and merging, reconfigurable polarity, transportation, self-assembly	both support high load capacity and achieve morphological adaptability	phase change time consuming

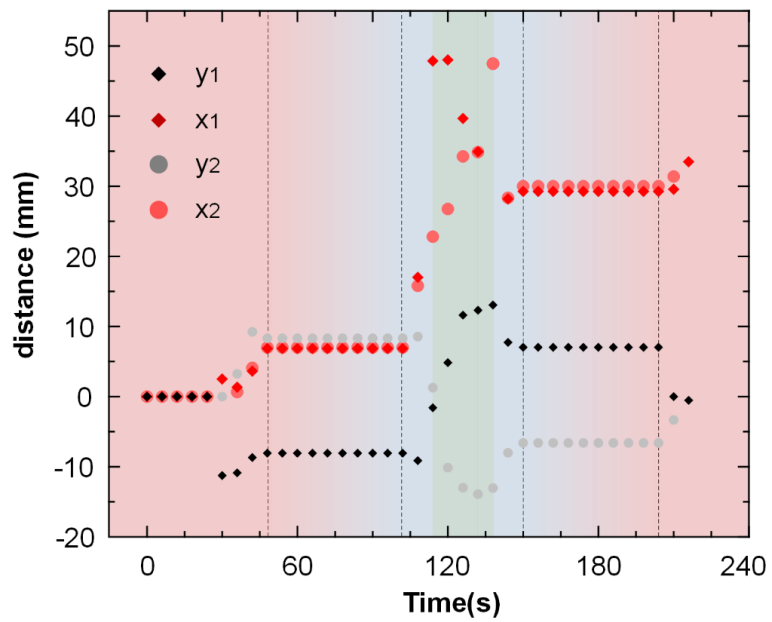


Figure S14. The displacement in the x and y directions of the MPTM changes with time.

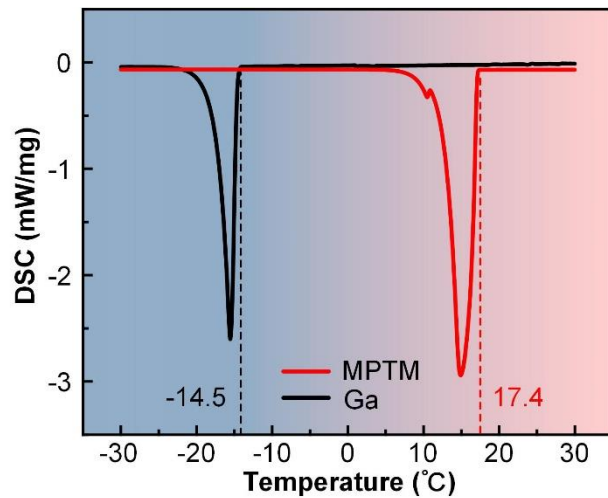


Figure S15. The cooling curves of MPTM and Ga using differential scanning calorimetry (DSC).

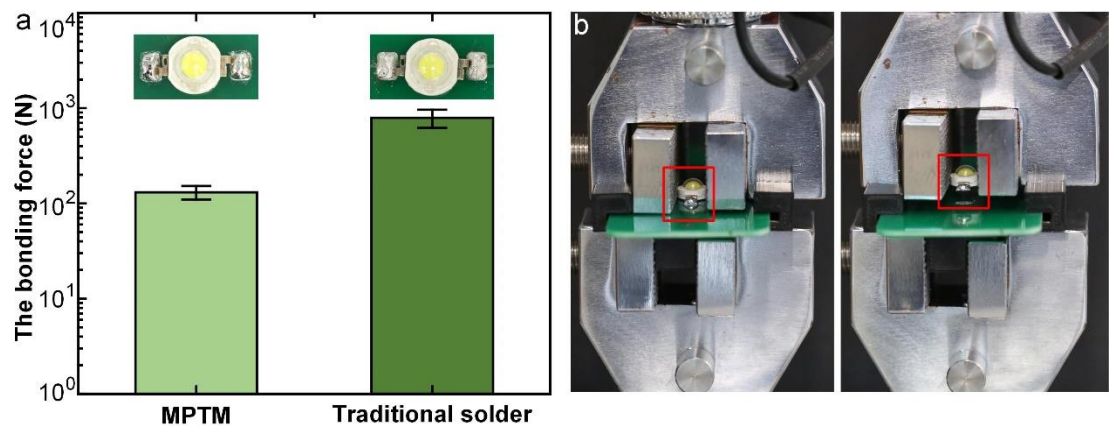


Figure S16. The bonding force of the MPTM as smart soldering machine. (a) The bonding force of the MPTM with traditional solder. (b) Bonding force testing with universal testing machine.

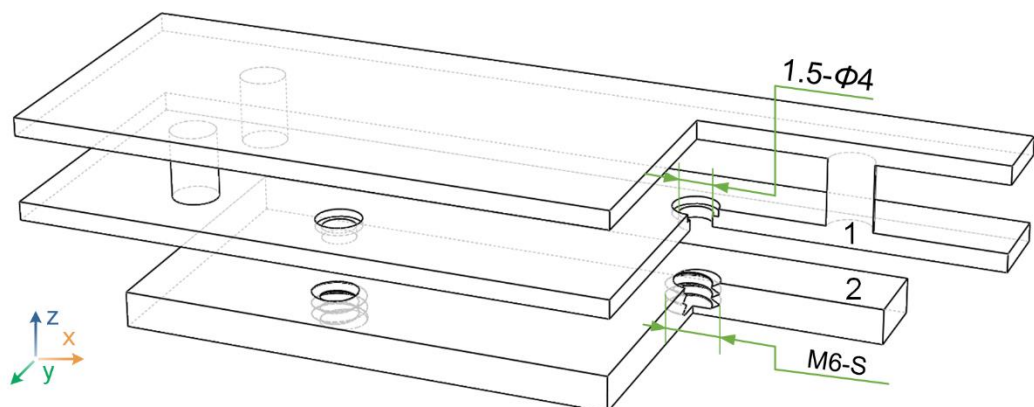


Figure S17. Structural drawings of the two parts.

Dimensions of thread are designed according to “GB/T 196-2003 General purpose metric screw threads--Basic dimensions”, and the screw threads in Figure 5e are marked as M3×0.8-S, M4×0.8-S, M5×0.8-S, M6×1.5-S, M7×1.5-S and M8×1.5-S, respectively.

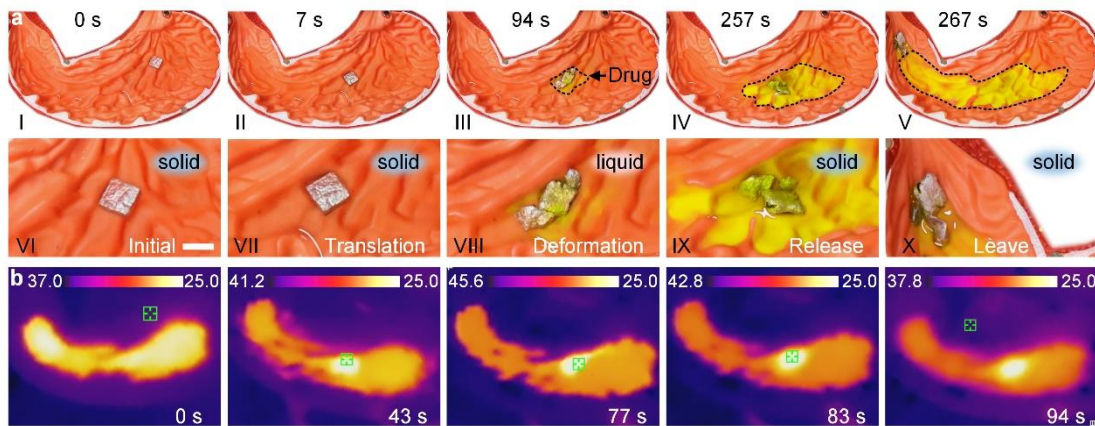


Figure S18. MPTM-46 for performing drug delivery. (a) Sequential Optical images and (b) infra-red images of the MPTM-46 drug delivery process. (Scale bars, 9 mm).

To see if the high-melting alloy could successfully release the drug, we use MPTM-46 instead of MPTM to demonstrate the experiments in the stomach model. MPTM-46 is made of the high melting point alloy ($\text{In}_{53}\text{Bi}_{25}\text{Sn}_{14}\text{Ga}_8$). The experimental results show that the MPTM-46 can be heated from 37 °C to 46 °C by AMF (Figure S18). Eventually, the MPTM-46 managed to release the drug.

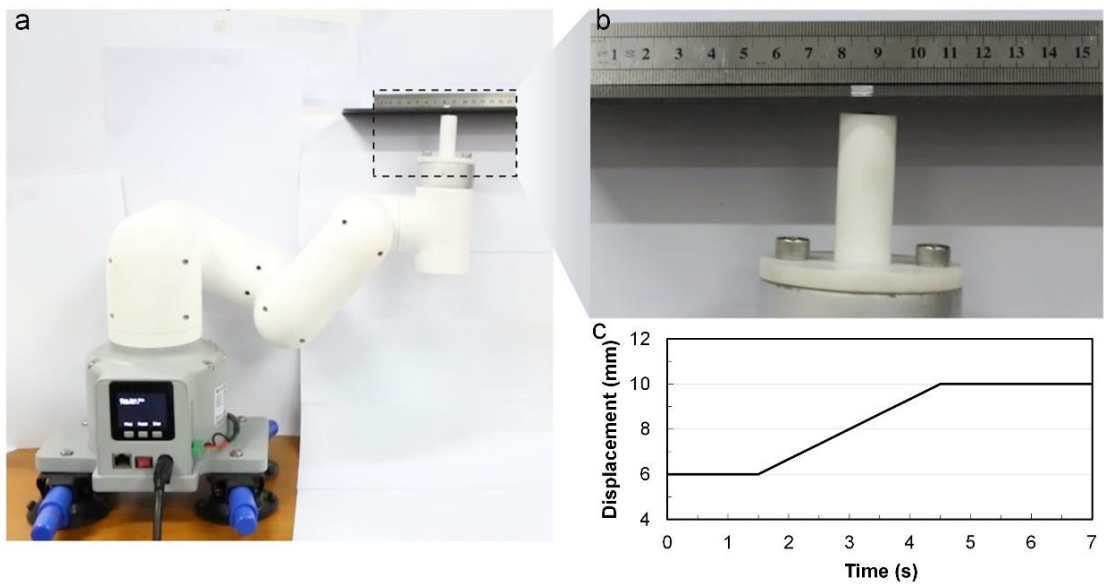


Figure S19. Magnetic manipulation platform based on permanent magnets. (a) Magnetic actuation and manipulation platforms based on permanent magnets. (b) MPTM moves following the permanent magnet. (c) The lateral coordinates of the robot change with time.

For more precise and reliable manipulation, we use a serial robot arm manipulator with multiple degrees of freedom (DOFs) to carry the actuating magnet and manipulate MPTM (Figure S19a). Under magnetic control, MPTM moves 40 mm at a speed of 0.8 m/min (Figure S19b-c).

References

S1. Aksoy, B., and Shea, H. (2022). Multistable shape programming of variable-stiffness electromagnetic devices. *Sci. Adv.* 8. 10.1126/sciadv.abk0543.

S2. Rich, S., Jang, S.-H., Park, Y.-L., and Majidi, C. (2017). Liquid Metal - Conductive Thermoplastic Elastomer Integration for Low - Voltage Stiffness Tuning. *Adv. Mater. Technol.* 2, 1. 10.1002/admt.201700179.

S3. Coulson, R., Stabile, C. J., Turner, K. T., and Majidi, C. (2022). Versatile Soft Robot Gripper Enabled by Stiffness and Adhesion Tuning via Thermoplastic Composite. *Soft Robot.* 9, 189. 10.1089/soro.2020.0088.

S4. Philen, M. (2010). Force Tracking Control of Fluidic Flexible Matrix Composite Variable Stiffness Structures. *J. Intell. Mater. Syst. Struct.* 22, 31. 10.1177/1045389X10391498.

S5. Kaufhold, T., Boehm, V., and Zimmermann, K. (2012). In Design of a Miniaturized Locomotion System with Variable Mechanical Compliance Based on Amoeboid Movement. presented at *4th IEEE RAS and EMBS International Conference on Biomedical Robotics and Biomechatronics (BioRob) / Symposium on Surgical Robotics*, Rome, ITALY, 1060-1065.

S6. Wu, J., Song, Z., Liu, F., Guo, J., Cheng, Y., Ma, S., and Xu, G. (2016). Giant electrorheological fluids with ultrahigh electrorheological efficiency based on a micro/nano hybrid calcium titanyl oxalate composite. *NPG Asia Mater.* 8, 322. 10.1038/am.2016.158.

S7. Li, Y., Maeda, Y., and Hashimoto, M. (2015). Lightweight, Soft Variable Stiffness Gel Spats for Walking Assistance. *International Journal Of Advanced Robotic Systems* 12, 175. 10.5772/61815.

S8. Tatari, M., Mohammadi Nasab, A., Turner, K. T., and Shan, W. (2018). Dynamically Tunable Dry Adhesion via Subsurface Stiffness Modulation. *ACS Appl. Mater. Interfaces* 5, 1800321. 10.1002/admi.201800321.

S9. Chen, Z., Lu, W., Li, Y., Liu, P., Yang, Y., and Jiang, L. (2022). Solid–Liquid State Transformable Magnetorheological Millirobot. *ACS Appl. Mater. Interfaces* 14(26), 30007-30020. 10.1021/acsami.2c05251.

S10. Zhang, J., Pang, H., Wang, Y., and Gong, X. (2020). The magneto-mechanical properties of off-axis anisotropic magnetorheological elastomers. *Compos. Sci. Technol.* 191, 108179. 10.1016/j.compscitech.2020.108079.

S11. Zhang, Y., Jiang, S., Hu, Y., Wu, T., Zhang, Y., Li, H., Li, A., Zhang, Y., Wu, H., Ding, Y., Li, E., Li, J., Wu, D., Song, Y., and Chu J. (2022). Reconfigurable Magnetic Liquid Metal Robot for High-Performance Droplet Manipulation. *Nano Lett.* 22(7), 2923-2933. 10.1021/acs.nanolett.2c00100.

S12. Li, X., Li, S., Lu, Y., Liu, M., Li, F., Yang, H., Tang, S. Y., Zhang, S., Li, W., and Sun, L. (2020). Programmable Digital Liquid Metal Droplets in Reconfigurable Magnetic Fields. *ACS Appl. Mater. Interfaces* 12, 37670. 10.1021/acsami.0c08179.

S13. He, X., Ni, M., Wu, J., Xuan, S., and Gong, X. (2021). Hard-magnetic liquid metal droplets with excellent magnetic field dependent mobility and elasticity. *J. Mater. Sci. Technol.* 92, 60. 10.1016/j.jmst.2021.04.004.

S14. Wang, H., Chen, S., Li, H., Chen, X., Cheng, J., Shao, Y., Zhang, C., Zhang, J., Fan, L., Chang, H., Guo, R., Wang, X., Li, N., Hu, L., Wei, Y., and Liu, J. (2021). A Liquid Gripper Based on Phase Transitional Metallic Ferrofluid. *Adv. Funct. Mater.* 31, 1. 10.1002/adfm.202100274.